Stereographic projection for three-dimensional global discontinuous Galerkin atmospheric modeling

Blaise, Sébastien; Lambrechts, Jonathan; Deleersnijder, ELC

DOI
10.1002/2015MS000428

Publication date
2015

Document Version
Final published version

Published in
Journal of Advances in Modeling Earth Systems

Citation (APA)
Blaise, S., Lambrechts, J., & Deleersnijder, ELC. (2015). Stereographic projection for three-dimensional global discontinuous Galerkin atmospheric modeling. *Journal of Advances in Modeling Earth Systems*, *2015*(7). https://doi.org/10.1002/2015MS000428

AGU PUBLICATIONS

Journal of Advances in Modeling Earth Systems

RESEARCH ARTICLE
10.1002/2015MS000428

Stereographic projection for three-dimensional global discontinuous Galerkin atmospheric modeling

Sébastien Blaise[1], Jonathan Lambrechts[1], and Eric Deleersnijder[2,3]

[1]Institute of Mechanics, Materials and Civil Engineering, Université catholique de Louvain, Louvain-la-Neuve, Belgium, [2]Institute of Mechanics, Materials and Civil Engineering and Earth and Life Institute, Université catholique de Louvain, Louvain-la-Neuve, Belgium, [3]Delft Institute of Applied Mathematics, Delft University of Technology, Delft, Netherlands

Key Points:
- A new approach for 3d global deep-atmospheric modeling on the sphere
- Mass-conservative approach, applicable to any discretization
- Complete validation with convergence analysis and comparisons

Correspondence to:
S. Blaise,
sebastien.blaise@uclouvain.be

Citation:
Blaise, S., J. Lambrechts, and E. Deleersnijder (2015), Stereographic projection for three-dimensional global discontinuous Galerkin atmospheric modeling, *J. Adv. Model. Earth Syst., 7*, 1026–1050, doi:10.1002/2015MS000428.

Received 9 JAN 2015
Accepted 9 JUN 2015
Accepted article online 13 JUN 2015
Published online 14 JUL 2015

Abstract A method to solve the three-dimensional compressible Navier-Stokes equations on the sphere is suggested, based on a stereographic projection with a high-order mapping of the elements from the stereographic space to the sphere. The projection is slightly modified, in order to take into account the domain thickness without introducing any approximation about the aspect ratio (deep-atmosphere). In a discontinuous Galerkin framework, the elements alongside the equator are exactly represented using a nonpolynomial geometry, in order to avoid the numerical issues associated with the seam connecting the two hemispheres. This is an crucial point, necessary to avoid mass loss and spurious deviations of the velocity. The resulting model is validated on idealized three-dimensional atmospheric test cases on the sphere, demonstrating the good convergence properties of the scheme, its mass conservation, and its satisfactory behavior in terms of accuracy and low numerical dissipation. A simulation is performed on a variable resolution unstructured grid, producing accurate results despite a substantial reduction of the number of elements.

1. Introduction

Thanks to its attractive properties such as parallel efficiency and the availability of high-order accurate schemes, the discontinuous Galerkin (DG) method is particularly well adapted to atmospheric dynamics. Several DG atmospheric models are currently under development [e.g., *St-Cyr and Neckels*, 2009; *Nair et al*., 2005; *Giraldo and Restelli*, 2008; *Giraldo et al*., 2010; *Brdar et al*., 2013; S. Blaise et al., A stable three-dimensional discontinuous Galerkin discretization for nonhydrostatic atmospheric simulations, International Journal for Numerical Methods in Fluids, submitted for publication, http://hdl.handle.net/2078.1/155002]. While a few DG models simulate geophysical flows on the sphere, they are still in active development, and generally not ready for climate or weather studies. The generalization of those models to realistic three-dimensional flows on the sphere is a very challenging and pressing task. The ability to solve flow equations on spherical domains is indeed an indispensable skill for global atmospheric and ocean models. However, despite the existence of various techniques developed to this aim, none of them can be considered entirely satisfactory.

Classical longitude-latitude grids are characterized by pole singularities requiring to be handled carefully [*Murray*, 1996; *Mohseni and Colonius*, 2000]. Indeed, the zonal grid spacing decreases toward zero as the poles are approached, causing efficiency issues. Such grids are also subject to stability restrictions, the stable explicit time step being directly proportional to the grid size. Thus, filters or stabilizations are usually needed in the vicinity of the poles [*Murray and Reason*, 2002]. More recent models, such as ENDGame from the UK MET Office, benefit from an improved stability at the poles, removing the need of polar filters in most cases [*Mayne et al*., 2014].

The most general and flexible method is probably the use of local tangent bases [*Comblen et al*., 2009; *Bernard et al*., 2009; *Blaise et al*., 2010; *Comblen et al*., 2010], allowing for the use of any type of mesh on a large class of curved manifolds. However, the vector fields need to be interpolated to and from the high-order tangent local bases, which requires additional computational effort, as well as a more complex implementation. The implementation of the coupling between elements is also made more complex by the different bases associated with each element.

A simplified approach, using only six local bases, is based upon the cubed sphere: the central projection of a cube onto the surface of the sphere [*Sadourny*, 1972; *Ronchi et al*., 1996]. It is one of the most popular methods used in the past years to simulate atmospheric flows on the sphere [*Nair et al*., 2005; *Dennis et al*., 2005;

Putman and Lin, 2007]. Six different coordinate systems associated with the faces of the cube are defined, to which correspond additional metric terms. Several versions of the cubed sphere have been developed, which may allow for the use of a conformal mapping [*Rančić et al*., 1996]. However, the corners of the cube correspond to singularities that must be handled with care [e.g., *Ivan et al*., 2013]. Furthermore, the alignment of the mesh, as well as the presence of the most distorted elements close to the corners, are likely to generate spurious modes or grid-related oscillations [*St-Cyr et al*., 2008; *Nair and Jablonowski*, 2008; *Lauritzen et al*., 2010].

Another simple method resorts to Lagrange multipliers: the equations are solved in a three-dimensional Cartesian space, and an additional constraint forces the fluid particles to remain on the surface of the sphere [*Côté*, 1988]. Regardless of the spatial discretization, it is probably the easiest way to transform an explicit two-dimensional planar model to a model operating on the sphere. The technique has been successfully used in the DG framework for two-dimensional flows [*Giraldo et al*., 2002; *Blaise and St-Cyr*, 2011; *Blaise et al*., 2013], and can be extended to three-dimensional flows [*Stuhne and Peltier*, 2006, 2009]. However, this approach requires the resolution of an additional equation for the momentum. Furthermore, enforcing the abovementioned constraint in an implicit framework is not straightforward.

An alternative approach is based upon the stereographic projection [*Snyder*, 1987]. The technique has been introduced during the early developments of geophysical models [*Phillips*, 1957]. However, the change of the grid size resulting from the projection makes it difficult to use efficiently methods such as finite differences, which do not provide enough flexibility on the mesh resolution. As a consequence, the stereographic projection was used in conjunction with a different coordinates system (e.g., Mercator), resulting in overlapping grids and associated numerical errors [*Phillips*, 1957; *Chen and Kuo*, 1986]. More recently, *Marras et al*. [2014] proposed to avoid overlapping grids by connecting the different subdomains using transition regions on which a transfinite interpolation was applied. However, this approach involves a domain division into 14 different regions associated with three different transformations, resulting in a more complex implementation.

Benefiting from the grid flexibility associated with the finite element method, *Düben et al*. [2012] proposed a two-dimensional discretization of the shallow water equations on the sphere using exclusively the stereographic coordinates. However, the stereographic projection involves a singularity, associated with the projection point at a pole. In order to map the whole sphere on a plane without singularity, it is necessary to split the spherical domain into its southern and northern hemispheres, each one being associated with a different projection point respectively located at the north and south pole. Doing so, *Düben et al*. [2012] observed a loss of global mass in their numerical simulations, caused by the inaccurate treatment of the seam coupling the two domains. Furthermore, they were able to obtain a stable model only by considering a linear mapping between the reference element on the plane and the element on the sphere, which is why they concluded that other methods should be considered for atmospheric simulations on global spherical domains.

In this study, we propose to use the stereographic projection with a high-order mapping of the elements from the stereographic space onto the sphere. The projection is slightly modified, in order to take into account the domain depth without introducing any approximation as to the aspect ratio (section 2). Based on their general expression in an orthogonal curvilinear system, the relevant differential operators are derived in the stereographic system of coordinates (section 3). Those operators are used to express in the same system the three-dimensional compressible Navier-Stokes equations, describing nonhydrostatic atmospheric flows (section 4), which are then discretized using the discontinuous Galerkin method (section 5). The elements alongside the equator are represented using a nonpolynomial geometry, so that the two subdomains match exactly, without hole or overlapping region (section 6). The method is then validated on classical three-dimensional atmospheric test cases on the sphere (section 7).

The approach proposed in this article has several advantages. It is simple: only two space transformations are considered, which can share a common implementation since they only differ by a sign. This implementation is straighforward, consisting in the addition of source terms to the equations, as well as the multiplication of integral and derivation operators by a simple factor. Further, the geometrical mapping associated with the elements located along the equator needs to be modified, a modification easily performed in a high-order (dis)continuous Galerkin based code. Despite this simplicity, no approximation is made about the aspect ratio (deep-atmosphere effects are considered), and mass is strictly conserved. Further, the overhead in computational time is negligible, since it is only due to a few additional source terms.

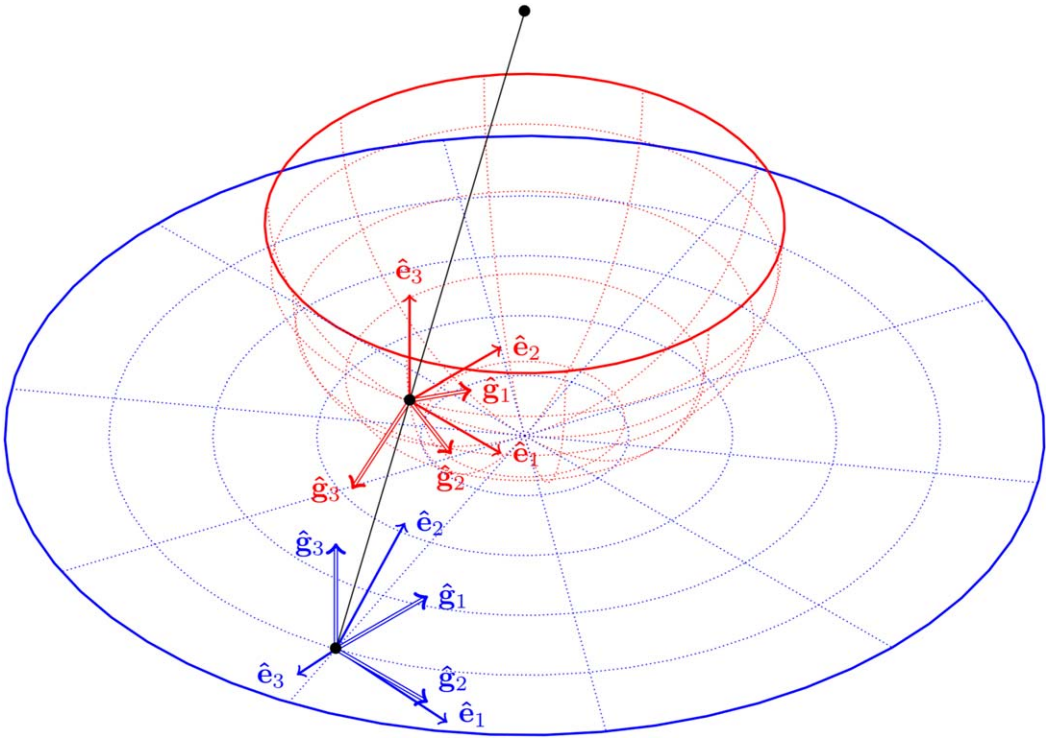

Figure 1. Stereographic projection of the southern hemisphere onto a plane. From top to bottom, the bullets along the line of projection represent the projection point (north pole), the point on the sphere to be projected and the projection of this point on the stereographic plane. The respective basis vectors of the Cartesian and the stereographic space $\hat{\mathbf{e}}_i$ (single lines) and $\hat{\mathbf{g}}_i$ (double lines) at the projection point are displayed in the Cartesian space (red) and the stereographic space (blue). Meridians and parallels, represented by dotted lines, are displayed for visualization purposes.

2. The Stereographic Transformation for Three-Dimensional Domains

The stereographic transformation projects a point from the surface of a sphere to a plane tangent to one of its poles, using a projection point located on the opposite pole (Figure 1). It has the advantage of being conformal (i.e., angles are preserved). However, the transformation is undefined at the projection point, making it impossible to map the whole sphere onto a plane. To circumvent this limitation, existing two-dimensional geophysical models [e.g., *Düben et al*., 2012] split the spherical domain into its southern and northern hemispheres, each one being associated with a different projection point respectively located at the north and south pole. As a result, each hemisphere is mapped onto a disk whose radius is twice that of the Earth.

However, in the case of a three-dimensional domain, the projection of a curved surface onto a plane surface is not adequate. Because of the atmosphere thickness, it is necessary to consider a mapping from a three-dimensional domain, lying in the Cartesian space of coordinates $\mathbf{x}=x_1\hat{\mathbf{e}}_1+x_2\hat{\mathbf{e}}_2+x_3\hat{\mathbf{e}}_3$, to another three-dimensional domain in the stereographic space of coordinates $\boldsymbol{\alpha}=\alpha_1\hat{\mathbf{g}}_1+\alpha_2\hat{\mathbf{g}}_2+\alpha_3\hat{\mathbf{g}}_3$, where $\hat{\mathbf{e}}_i$ and $\hat{\mathbf{g}}_i$ are the respective basis vectors of the Cartesian and the stereographic spaces. Such a mapping, whose vertical structure is illustrated by Figure 2, can be obtained through an appropriate modification of the stereographic transformation:

$$\begin{cases} x_1(\alpha_1,\alpha_2,\alpha_3) &= \dfrac{R+\alpha_3}{R}\dfrac{4R^2\alpha_1}{4R^2+\alpha_1^2+\alpha_2^2}, \\ x_2(\alpha_1,\alpha_2,\alpha_3) &= \dfrac{R+\alpha_3}{R}\dfrac{4R^2\alpha_2}{4R^2+\alpha_1^2+\alpha_2^2}, \\ x_3(\alpha_1,\alpha_2,\alpha_3) &= \pm(R+\alpha_3)\dfrac{4R^2-\alpha_1^2-\alpha_2^2}{4R^2+\alpha_1^2+\alpha_2^2}, \end{cases} \tag{1}$$

where R is the Earth radius while the $\pm$ sign is related to the hemisphere under consideration ($+$ for the north and – for the south). This relation corresponds to the classical stereographic transformation for a shell, with the right-hand side multiplied by the factor $\frac{R+\alpha_3}{R}$ to account for the depth of the atmosphere. Hence, it

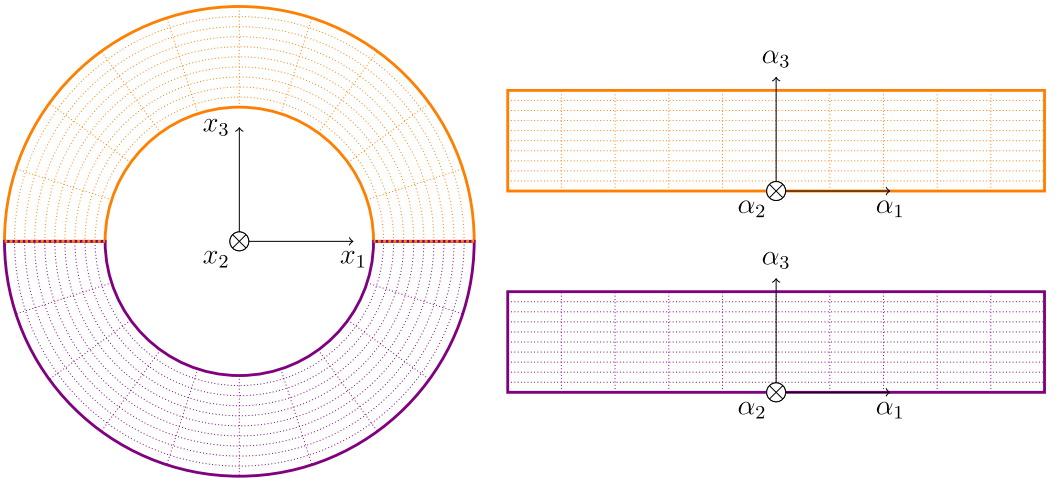

Figure 2. Slice at $x_2=\alpha_2=0$ of a three-dimensional global atmospheric domain in the (left) Cartesian and (right) stereographic spaces. Parallels and height isovalues, represented by dotted lines, are displayed for visualization purposes.

is possible to obtain the classical projection by prescribing $\alpha_3=0$, resulting in the projection of the spherical surface onto a disk (Figure 1). The mapping (1) preserves a conformal character without introducing any approximation as to the aspect ratio (i.e., no shallow-atmosphere approximation).

The basis vectors of the stereographic space $\hat{\mathbf{g}}_i$ expressed in terms of those defining the Cartesian basis $\hat{\mathbf{e}}_i$ are obtained through the differentiation of (1) with respect to the coordinates of the stereographic space:

$$\begin{cases} \hat{\mathbf{g}}_1=\dfrac{1}{h_1}\dfrac{\partial \mathbf{x}(\alpha_1,\alpha_2,\alpha_3)}{\partial \alpha_1}=\dfrac{1}{h_1}\left(\dfrac{4R(R+\alpha_3)\left(4R^2-{\alpha_1}^2+{\alpha_2}^2\right)}{\left(4R^2+{\alpha_1}^2+{\alpha_2}^2\right)^2}\hat{\mathbf{e}}_1-\dfrac{8R\alpha_1\alpha_2(R+\alpha_3)}{\left(4R^2+{\alpha_1}^2+{\alpha_2}^2\right)^2}\hat{\mathbf{e}}_2\mp\dfrac{16R^2\alpha_1(R+\alpha_3)}{\left(4R^2+{\alpha_1}^2+{\alpha_2}^2\right)^2}\hat{\mathbf{e}}_3\right), \\ \hat{\mathbf{g}}_2=\dfrac{1}{h_2}\dfrac{\partial \mathbf{x}(\alpha_1,\alpha_2,\alpha_3)}{\partial \alpha_2}=\dfrac{1}{h_2}\left(-\dfrac{8R\alpha_1\alpha_2(R+\alpha_3)}{\left(4R^2+{\alpha_1}^2+{\alpha_2}^2\right)^2}\hat{\mathbf{e}}_1+\dfrac{4R(R+\alpha_3)\left(4R^2+{\alpha_1}^2-{\alpha_2}^2\right)}{\left(4R^2+{\alpha_1}^2+{\alpha_2}^2\right)^2}\hat{\mathbf{e}}_2\mp\dfrac{16R^2\alpha_2(R+\alpha_3)}{\left(4R^2+{\alpha_1}^2+{\alpha_2}^2\right)^2}\hat{\mathbf{e}}_3\right), \\ \hat{\mathbf{g}}_3=\dfrac{1}{h_3}\dfrac{\partial \mathbf{x}(\alpha_1,\alpha_2,\alpha_3)}{\partial \alpha_3}=\dfrac{1}{h_3}\left(\dfrac{4R\alpha_1}{4R^2+{\alpha_1}^2+{\alpha_2}^2}\hat{\mathbf{e}}_1+\dfrac{4R\alpha_2}{4R^2+{\alpha_1}^2+{\alpha_2}^2}\hat{\mathbf{e}}_2\pm\dfrac{4R^2-\alpha_1^2-\alpha_2^2}{4R^2+{\alpha_1}^2+{\alpha_2}^2}\hat{\mathbf{e}}_3\right), \end{cases} \tag{2}$$

where h_1, h_2 and h_3 are the so-called scale factors or Lamé coefficients [*Lamé*, 1859; *Chen et al.*, 1996], whose values are defined in such a way that the basis vectors have a unit norm:

$$h_1=h_2=\frac{4R(R+\alpha_3)}{4R^2+\alpha_1^2+\alpha_2^2}\quad h_3=1. \tag{3}$$

Since the orthogonality of the basis vectors $\hat{\mathbf{g}}_1$, $\hat{\mathbf{g}}_2$ and $\hat{\mathbf{g}}_3$ at any point is easily verified, the basis (2) is associated with an orthogonal curvilinear coordinate system.

3. Three-Dimensional Differential Operators in Stereographic Coordinates

For orthogonal curvilinear coordinates systems, the differential operators can be expressed in terms of the scale factors, as has been done in the literature [e.g., *Kemmer*, 1977; *Martinec*, 2003]. Those expressions are useful to rewrite each term of a differential equation in the stereographic coordinate system.

The divergence of a vector $\boldsymbol{v}=v_1\hat{\mathbf{g}}_1+v_2\hat{\mathbf{g}}_2+v_3\hat{\mathbf{g}}_3$ defined in an orthogonal curvilinear system of coordinates reads [*Martinec*, 2003]

$$\nabla\cdot\boldsymbol{v}=\frac{1}{h_1h_2h_3}\left(\frac{\partial(h_2h_3v_1)}{\partial\alpha_1}+\frac{\partial(h_1h_3v_2)}{\partial\alpha_2}+\frac{\partial(h_1h_2v_3)}{\partial\alpha_3}\right), \tag{4}$$

which can be expressed in stereographic coordinates using (3):

$$\nabla \cdot \boldsymbol{v} = \frac{1}{J}\frac{\partial v_1}{\partial \alpha_1} + \frac{1}{J}\frac{\partial v_2}{\partial \alpha_2} + \frac{\partial v_3}{\alpha_3} + \frac{1}{R+\alpha_3}\left(2v_3 - \frac{\alpha_1 v_1 + \alpha_2 v_2}{2R}\right), \tag{5}$$

where J is defined to be $J = h_1 = h_2$. Note that expression (5) with $\alpha_3 = v_3 = 0$ corresponds to the divergence written in the original stereographic coordinates, as described by *Düben et al*. [2012]. The gradient of a scalar s in curvilinear orthogonal coordinates is obtained similarly:

$$\nabla s = \sum_k \frac{1}{h_k}\frac{\partial s}{\partial \alpha_k} = \begin{pmatrix} \frac{1}{J}\frac{\partial s}{\partial \alpha_1} \\ \frac{1}{J}\frac{\partial s}{\partial \alpha_2} \\ \frac{\partial s}{\partial \alpha_3} \end{pmatrix}. \tag{6}$$

According to *Martinec* [2003], the divergence of a tensor can be evaluated as follows

$$\nabla \cdot \boldsymbol{T} = \sum_{kl}\frac{1}{h_k}\left(\frac{\partial T_{kl}}{\partial \alpha_k} + \sum_{m\neq k}\frac{1}{h_m}\frac{\partial h_k}{\partial \alpha_m}\right)\hat{\mathbf{g}}_l + \sum_l \sum_{k\neq l}\frac{1}{h_k h_l}\left(\frac{\partial h_l}{\partial \alpha_k}T_{lk} - \frac{\partial h_k}{\partial \alpha_l}T_{kk}\right)\hat{\mathbf{g}}_l, \tag{7}$$

where T_{kl} refers to the entry of the tensor $\boldsymbol{T}$ corresponding to line k and column l. Each component of the gradient of a vector is

$$(\nabla \boldsymbol{v})_{kl} = \begin{cases} \frac{1}{h_k}\left(\frac{\partial u_k}{\partial \alpha_k} + \sum_m \frac{1}{h_m}\frac{\partial h_k}{\partial \alpha_m}u_m\right) & \text{if } l = k, \\ \frac{1}{h_k}\left(\frac{\partial u_l}{\partial \alpha_k} - \frac{1}{h_l}\frac{\partial h_k}{\partial \alpha_l}u_k\right) & \text{if } l \neq k. \end{cases} \tag{8}$$

4. Three-Dimensional Equations in Stereographic Coordinates

The three-dimensional compressible Navier-Stokes equations, describing nonhydrostatic atmospheric processes [e.g., *Giraldo and Restelli*, 2008; Blaise et al., submitted manuscript, 2015], are considered as the starting point. Simplified diffusion terms, with a diagonal diffusion tensor when expressed in in the stereographic basis $\boldsymbol{D} = \mathrm{diag}(\kappa_h, \kappa_h, \kappa_v)$, are considered [*Straka et al*., 1993; *Jacobson*, 2005]. Coriolis effect has been added to take into account the Earth rotation around its axis with an angular velocity $\boldsymbol{\omega}$:

$$\frac{\partial \rho'}{\partial t} + \nabla \cdot (\rho \mathbf{u}) = 0 \tag{9a}$$

$$\frac{\partial \rho \mathbf{u}}{\partial t} + \nabla \cdot (\rho \mathbf{u}\,\mathbf{u} + p'\mathbb{I}) + \rho' g \hat{\mathbf{g}}_3 - \nabla \cdot (\rho \boldsymbol{D} \cdot \nabla \mathbf{u}) + 2\rho\,\boldsymbol{\omega} \times \mathbf{u} = 0 \tag{9b}$$

$$\frac{\partial (\rho\theta)'}{\partial t} + \nabla \cdot (\rho\theta \mathbf{u}) - \nabla \cdot (\rho \boldsymbol{D} \cdot \nabla \theta) = 0 \tag{9c}$$

where ρ is the density, θ is the potential temperature, and $\mathbf{u} = [u_1, u_2, u_3]$ is the velocity vector. The gravitational acceleration is denoted g while $\mathbb{I} = \mathrm{diag}(1,1,1)$ is the identity matrix of size 3. Equations (9) are written in terms of deviations from a reference state, such that the prime symbol refers to a perturbation of a variable around a background value (overlined), which is in hydrostatic balance (for details, see *Giraldo and Restelli* [2008]):

$$\rho'(\mathbf{x}, t) = \rho(\mathbf{x}, t) - \bar{\rho}(z), \tag{10a}$$

$$(\rho\theta)'(\mathbf{x}, t) = (\rho\theta)(\mathbf{x}, t) - \overline{\rho\theta}(z). \tag{10b}$$

The pressure perturbation p' in the momentum equation is obtained from

$$p' = p_0 \left(\frac{\rho\theta R_d}{p_0} \right)^{\frac{c_p}{c_v}} - p_0 \left(\frac{\overline{\rho\theta} R_d}{p_0} \right)^{\frac{c_p}{c_v}}, \tag{11}$$

where $p_0 = 10^5$ Pa is the reference surface pressure, $R_d = c_p - c_v$ is the gas constant, while c_p and c_v are the specific heat of the air at constant pressure and volume.

4.1. Continuity Equation

Using the expression for the divergence of a vector in the stereographic space (5), it is straightforward to express the divergence of $\rho\mathbf{u}$ from the continuity equation (9a) in stereographic coordinates:

$$\nabla \cdot (\rho\mathbf{u}) = \frac{1}{J}\frac{\partial(\rho u_1)}{\partial\alpha_1} + \frac{1}{J}\frac{\partial(\rho u_2)}{\partial\alpha_2} + \frac{\partial(\rho u_3)}{\partial\alpha_3} + \frac{1}{R+\alpha_3}\left(2\rho u_3 - \frac{\alpha_1\rho u_1 + \alpha_2\rho u_2}{2R} \right). \tag{12}$$

The first three terms of the right-hand side correspond to the classical divergence of $\rho\mathbf{u}$, except for a scaling factor J taking into account the horizontal stretching of the domain associated with the coordinate transformation. The source terms are related to the curvature of the sphere. The complete expression of the equations in the stereographic basis, including all the terms of equations (9), can be found in Appendix A.

4.2. Momentum Equation

The momentum equation (9b) involves the divergence of tensor fields, and is the most delicate to handle. The scale factors associated with the stereographic transformation (3) are introduced in the expression of the divergence of a tensor in the stereographic space (7) to derive the advection term:

$$\begin{aligned} \nabla \cdot (\rho\mathbf{u}\,\mathbf{u}) = {} & \frac{1}{J}\frac{\partial}{\partial\alpha_1}\begin{pmatrix} \rho u_1^2 \\ \rho u_1 u_2 \\ \rho u_1 u_3 \end{pmatrix} + \frac{1}{J}\frac{\partial}{\partial\alpha_2}\begin{pmatrix} \rho u_1 u_1 \\ \rho u_2^2 \\ \rho u_2 u_3 \end{pmatrix} + \frac{\partial}{\partial\alpha_3}\begin{pmatrix} \rho u_1 u_3 \\ \rho u_2 u_3 \\ \rho u_3^2 \end{pmatrix} \\ & + \frac{\rho}{R+\alpha_3}\begin{pmatrix} 3u_1u_3 - \frac{u_1}{2R}(\alpha_1 u_1 + 2\alpha_2 u_2) + \frac{\alpha_1 u_2^2}{2R} \\ 3u_2u_3 - \frac{u_2}{2R}(\alpha_2 u_2 + 2\alpha_1 u_1) + \frac{\alpha_2 u_1^2}{2R} \\ 2u_3^2 - u_1^2 - u_2^2 - \frac{u_3}{2R}(\alpha_1 u_1 + \alpha_2 u_2) \end{pmatrix}, \end{aligned} \tag{13}$$

and the pressure term:

$$\nabla \cdot (p'\mathbb{I}) = \begin{pmatrix} \frac{1}{J}\frac{\partial p'}{\partial\alpha_1} \\ \frac{1}{J}\frac{\partial p'}{\partial\alpha_2} \\ \frac{\partial p'}{\partial\alpha_3} \end{pmatrix}. \tag{14}$$

As for the continuity equations, the three first terms of the right-hand side of (13) correspond to the classical advection term except from the scaling factor J.

Associating the gradient of a vector (8) with the divergence of a tensor (7) in the diffusion term of the momentum equation (9b) leads to

$$\nabla\cdot(\rho\boldsymbol{D}\cdot\nabla\mathbf{u})=\begin{pmatrix}\frac{1}{J^2}\frac{\partial\left(\rho\kappa_h\frac{\partial}{\partial\alpha_1}\right)}{\partial\alpha_1}+\frac{1}{J^2}\frac{\partial\left(\rho\kappa_h\frac{\partial}{\partial\alpha_2}\right)}{\partial\alpha_2}+\frac{\partial\left(\rho\kappa_v\frac{\partial}{\partial\alpha_3}\right)}{\partial\alpha_3}\end{pmatrix}\begin{pmatrix}u_1\\u_2\\u_3\end{pmatrix}$$
$$+\frac{1}{J(R+\alpha_3)}\begin{pmatrix}\frac{\partial(\rho\kappa_h u_3)}{\partial\alpha_1}+\rho\kappa_h\frac{\partial u_3}{\partial\alpha_1}+\frac{u_2}{2R}\left(\alpha_2\frac{\partial(\rho\kappa_h)}{\partial\alpha_1}-\alpha_1\frac{\partial(\rho\kappa_h)}{\partial\alpha_2}\right)+\frac{1}{R}\left(\alpha_1\frac{\partial(u_2\rho\kappa_h)}{\partial\alpha_2}-\alpha_2\frac{\partial(u_2\rho\kappa_h)}{\partial\alpha_1}\right)\\\frac{\partial(\rho\kappa_h u_3)}{\partial\alpha_2}+\rho\kappa_h\frac{\partial u_3}{\partial\alpha_2}+\frac{u_1}{2R}\left(\alpha_1\frac{\partial(\rho\kappa_h)}{\partial\alpha_2}-\alpha_2\frac{\partial(\rho\kappa_h)}{\partial\alpha_1}\right)+\frac{1}{R}\left(\alpha_2\frac{\partial(u_1\rho\kappa_h)}{\partial\alpha_1}-\alpha_1\frac{\partial(u_1\rho\kappa_h)}{\partial\alpha_2}\right)\\-\frac{\partial(\rho\kappa_h u_1)}{\partial\alpha_1}-\frac{\partial(\rho\kappa_h u_2)}{\partial\alpha_2}-\rho\kappa_h\left(\frac{\partial u_1}{\partial\alpha_1}+\frac{\partial u_2}{\partial\alpha_2}\right)\end{pmatrix}$$
$$+\frac{\rho}{R+\alpha_3}\begin{pmatrix}2\kappa_v\frac{\partial u_1}{\partial\alpha_3}-\frac{\kappa_h u_1}{R+\alpha_3}\left(1+\frac{\alpha_1^2+\alpha_2^2}{4R^2}\right)\\2\kappa_v\frac{\partial u_2}{\partial\alpha_3}-\frac{\kappa_h u_2}{R+\alpha_3}\left(1+\frac{\alpha_1^2+\alpha_2^2}{4R^2}\right)\\2\kappa_v\frac{\partial u_3}{\partial\alpha_3}+\frac{1}{R+\alpha_3}\left(\frac{\kappa_h}{R}(\alpha_1u_1+\alpha_2u_2)-2\kappa_h u_3\right)\end{pmatrix}. \tag{15}$$

While the expression appears to be quite long and complex, the difference with the classical diffusion in a Cartesian coordinate system consists in additional source terms, which are rather easy to implement.

4.3. Potential Temperature Equation

The expression of the divergence of a vector in the stereographic space (5) is used once again to express the first term of the potential temperature equation (9c) in stereographic coordinates:

$$\nabla\cdot(\rho\theta\mathbf{u})=\frac{1}{J}\frac{\partial(\rho\theta u_1)}{\partial\alpha_1}+\frac{1}{J}\frac{\partial(\rho\theta u_2)}{\partial\alpha_2}+\frac{\partial(\rho\theta u_3)}{\partial\alpha_3}+\frac{\rho}{R+\alpha_3}\left(2\theta u_3-\frac{\alpha_1\theta u_1+\alpha_2\theta u_2}{2R}\right). \tag{16}$$

For the diffusion term, it is necessary to combine the divergence of a vector (5) with the gradient of a scalar (8) in the stereographic space, leading to

$$\nabla\cdot(\rho\boldsymbol{D}\cdot\nabla\theta)=\frac{1}{J}\frac{\partial\left(\frac{\rho\kappa_h}{J}\frac{\partial\theta}{\partial\alpha_1}\right)}{\partial\alpha_1}+\frac{1}{J}\frac{\partial\left(\frac{\rho\kappa_h}{J}\frac{\partial\theta}{\partial\alpha_2}\right)}{\partial\alpha_2}+\frac{\partial\left(\rho\kappa_v\frac{\partial\theta}{\partial\alpha_3}\right)}{\partial\alpha_3}+\frac{\rho}{R+\alpha_3}\left(2\kappa_v\frac{\partial\theta}{\partial\alpha_3}-\kappa_h\frac{\alpha_1\frac{\partial\theta}{\partial\alpha_1}+\alpha_2\frac{\partial\theta}{\partial\alpha_2}}{2RJ}\right). \tag{17}$$

5. Discontinuous Galerkin Formulation

The discrete formulation of a discontinuous Galerkin model [e.g., *Giraldo and Restelli*, 2008] does not require any fundamental modification in order to be adapted to a spherical domain. The discretization of the continuity equation is considered here as an example of the changes to be performed in an existing code. The weak formulation of the continuity equation in stereographic coordinates (12) is obtained by multiplying this equation by a set of test functions and integrating over the elements. Upon doing so, a local problem has to be solved for each element Ω_e and test function ϕ_i:

$$\int_{\Omega_e}\phi_i\left(\frac{1}{J}\left(\frac{\partial u_1}{\partial\alpha_1}+\frac{\partial u_2}{\partial\alpha_2}\right)+\frac{\partial u_3}{\partial\alpha_3}\right)\mathrm{d}x_1\mathrm{d}x_2\mathrm{d}x_3$$
$$+\int_{\Omega_e}\frac{\phi_i}{R+\alpha_3}\left(2u_3-\frac{\alpha_1u_1+\alpha_2u_2}{2R}\right)\mathrm{d}x_1\mathrm{d}x_2\mathrm{d}x_3. \tag{18}$$

However, as for the differential operators, the integrals need to be expressed in the stereographic space in which the mesh is defined. The correspondence between the integrals is easily obtained, by resorting to the scale factors characterizing the change of length associated with the transformation:

$$\mathrm{d}x_1=h_1\mathrm{d}\alpha_1=J\mathrm{d}\alpha_1, \tag{19a}$$

$$dx_2 = h_2 d\alpha_2 = J d\alpha_2, \tag{19b}$$

$$dx_3 = h_3 d\alpha_3 = d\alpha_3. \tag{19c}$$

Introducing $d\Omega = d\alpha_1 d\alpha_2 d\alpha_3$ for brevity, the resulting weak formulation becomes

$$\int_{\Omega_e} J^2 \phi_i \left(\frac{1}{J} \left(\frac{\partial u_1}{\partial \alpha_1} + \frac{\partial u_2}{\partial \alpha_2} \right) + \frac{\partial u_3}{\partial \alpha_3} \right) d\Omega + \int_{\Omega_e} \frac{J^2 \phi_i}{R + \alpha_3} \left(2u_3 - \frac{\alpha_1 u_1 + \alpha_2 u_2}{2R} \right) d\Omega. \tag{20}$$

Following the discontinuous Galerkin procedure, an integration by parts is performed, leading to

$$\begin{aligned} \int_{\Omega_e} J^2 \phi_i \frac{\partial \rho'}{\partial t} d\Omega = &- \int_{\Omega_e} \left(\frac{\partial (J\phi_i)}{\partial \alpha_1} u_1 + \frac{\partial (J\phi_i)}{\partial \alpha_2} u_2 + \frac{\partial (J^2 \phi_i)}{\partial \alpha_3} u_3 \right) d\Omega \\ &+ \int_{\Gamma_e} \left(J\phi_i (u_1 n_1 + u_2 n_2) + J^2 \phi_i u_3 n_3 \right) d\Gamma \\ &+ \int_{\Omega_e} \frac{J^2 \phi_i}{R + \alpha_3} \left(2u_3 - \frac{\alpha_1 u_1 + \alpha_2 u_2}{2R} \right) d\Omega, \end{aligned} \tag{21}$$

where Γ_e is the exterior surface of Ω_e and n_1, n_2 and n_3 are the components of the outward-pointing normal to the element face. After some manipulations, the derivatives of the scaling factor J appear, which can be obtained analytically from (3):

$$\frac{\partial J}{\partial \alpha_1} = - \frac{J^2 \alpha_1}{2R(R + \alpha_3)}, \tag{22a}$$

$$\frac{\partial J}{\partial \alpha_2} = - \frac{J^2 \alpha_2}{2R(R + \alpha_3)}, \tag{22b}$$

$$\frac{\partial J}{\partial \alpha_3} = \frac{J}{R + \alpha_3}. \tag{22c}$$

Introducing those derivatives in (21) makes the source terms vanish, leading to

$$\begin{aligned} \int_{\Omega_e} J^2 \phi_i \frac{\partial \rho'}{\partial t} d\Omega = &- \int_{\Omega_e} \left(J \frac{\partial \phi_i}{\partial \alpha_1} u_1 + J \frac{\partial \phi_i}{\partial \alpha_2} u_2 + J^2 \frac{\partial \phi_i}{\partial \alpha_3} u_3 \right) d\Omega \\ &+ \int_{\Gamma_e} \left(J\phi_i (u_1 n_1 + u_2 n_2) + J^2 \phi_i u_3 n_3 \right) d\Gamma, \end{aligned} \tag{23}$$

which is the same as the classical weak formulation in Cartesian coordinates, except for the scaling factors *J*. As regards the implementation, it is possible to include those factors *J* in the routines computing the integral and derivation operators (e.g., multiply by J^2 each function to be integrated over the volume, divide by *J* each horizontal derivative). Doing so, the part of the code describing the discrete continuity equation remains unchanged from its Cartesian version. Note that source terms do not vanish completely for the momentum equation, but are reduced to simpler expressions.

6. Meshing a Disc

For large-scale numerical weather prediction, it is desireable that the equator coincides with a grid coordinate line [*Phillips*, 1957; *Ronchi et al*., 1996], although this is not an essential requirement [see e.g., *Zängl et al*., 2015]; *Majewski et al*., 2002]. The double stereographic projection with a seam at the equator described in section 2 fulfills this condition. The two subdomains in the stereographic space are cylinders whose radius is twice the Earth radius and height corresponds to the atmosphere depth. Given the high contrast between horizontal and vertical dynamics associated with atmospheric flows, we consider a three-dimensional mesh obtained from the extrusion over the vertical of a two-dimensional mesh. The latter consists of two circles, each one being associated with a different hemisphere with their outer boundary corresponding to the equator (Figure 1). For finite element meshes, the geometry of the domain is usually approximated with polynomials. It is then impossible to represent exactly a circle, and the resulting computational mesh does not cover the entire spherical domain (see Figure 3 for a linear discretization).

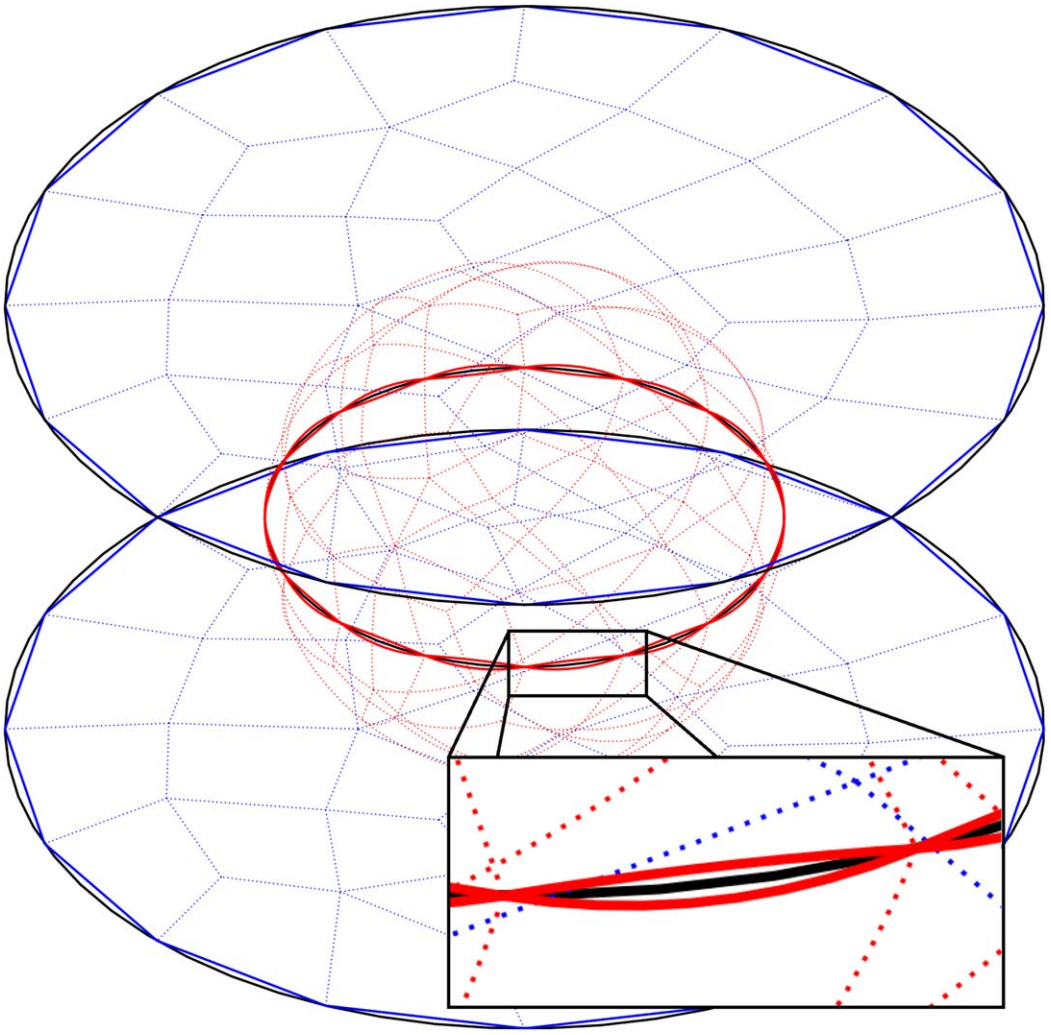

Figure 3. Stereographic mapping of two discs approximated using linear elements. The resulting sphere exhibits holes distributed along the equator. An example of mesh is represented by dotted lines in the stereographic (blue) and Cartesian (red) spaces.

While finer meshes and higher polynomial order approximations reduce considerably the geometrical error, the use of a simply connected approximation of the surface of the sphere is very important when using a finite element discretization. Indeed, as observed by *Düben et al*. [2012], computations performed on a non-simply connected mesh result in inconsistencies and mass loss.

While finite element codes usually consider polynomial approximations for the geometry, this is not a requirement of the method, even if the field variables are represented using a polynomial basis. The seam can be exactly represented, using circle-shaped edges to describe the equator line. For quadrilateral elements (other type of elements such as triangles could also be considered), classical models rely on a mapping between a reference square element of length 2 and the actual geometry of the quadrilateral in the mesh. To represent exactly the circle, a different transformation from the coordinates in the reference element (ξ,η) to the coordinates in the stereographic space $\boldsymbol{\alpha}$ is used for the elements that are adjacent to the disc boundary. This mapping, based upon the transfinite interpolation, can be applied in 4 steps (Figure 4):

$$\mathbf{P}_{12}=\frac{1+\xi}{2}\mathbf{P}_2+\frac{1-\xi}{2}\mathbf{P}_1, \tag{24a}$$

$$\hat{\mathbf{P}}_{12}=\frac{\mathbf{P}_{12}}{||\mathbf{P}_{12}||}, \tag{24b}$$

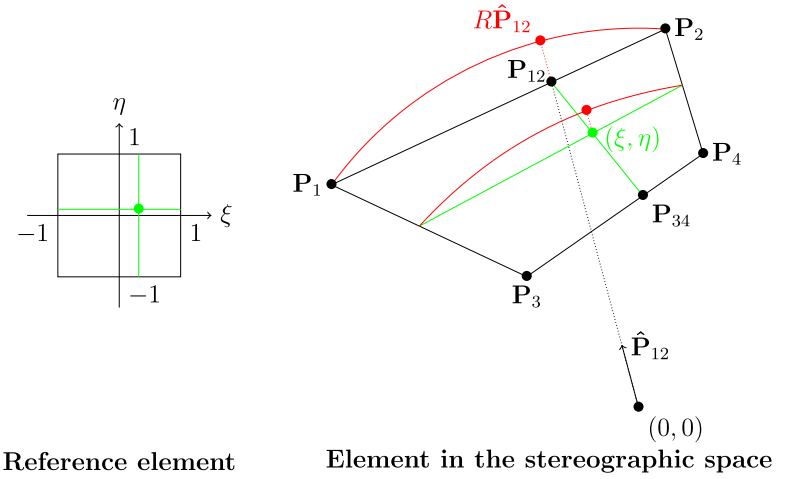

Figure 4. Transformation of a linear element (black) into an element whose an edge is a circle arc (red). Any point (green), of coordinates (ξ,η) in the reference element, is directly mapped to the transformed element using a transfinite interpolation.

$$\mathbf{P}_{34}=\frac{1+\xi}{2}\mathbf{P}_4+\frac{1-\xi}{2}\mathbf{P}_3, \tag{24c}$$

$$\boldsymbol{\alpha}=\frac{1+\eta}{2}R\hat{\mathbf{P}}_{12}+\frac{1-\eta}{2}\mathbf{P}_{34}. \tag{24d}$$

Unlike other possible transformations, this mapping has a unique projection point, ensuring that the way in which a node located on the seam is projected only depends on its position on the circle. This is an important property since the edges shared between two elements of different hemispheres need to be projected in the same manner on both sides.

Starting from (24), the mapping of the integration and differentiation operators from the reference element to the curved element can be easily derived and included in the code to replace those associated with the classical isomorphism.

Note that numerical spatial integration on those nonpolynomial elements cannot be performed exactly using classical Gauss-type methods. However, it will be seen in the next section that the quality of the solution is not degraded in practice: a Gauss-Legendre quadrature rule of order $2P+3$ is used without any trouble, P being the polynomial order of the finite element shape functions. It should be noted that exact Gauss-Legendre integration cannot be performed for any discretization involving a projection of the sphere, because of its nonpolynomial character.

7. Model Validation

The first part of this section briefly describes the model used for the validation of the method. This validation is then performed through several test cases. The first one is a three-dimensional transport test case, for which the analytical solution at the final time is known [*Kent et al.*, 2014]. Then, a more complete benchmark, for which an analytical solution is also available, is considered: the global propagation of gravity waves over the whole sphere [*Baldauf et al.*, 2014]. The model is then used for a more complex and widely used benchmark, namely the evolution of an idealized baroclinic wave in the northern hemisphere [*Jablonowski and Williamson*, 2006]. Finally, a generalization of the baroclinic wave benchmark, including deep-atmosphere dynamics, is considered in order to validate the deep-atmosphere component of the model, as well as its conservation properties [*Ullrich et al.*, 2013]. To facilitate the prescription of initial conditions expressed in the Cartesian or Longitude/Latitude system of coordinates, the transformation of vectors between different spaces are provided in Appendix B.

7.1. Model Description

The model used for the validation of the technique is a nonhydrostatic model based on the compressible Navier-Stokes equations (9). It relies upon a high-order nodal discontinuous Galerkin discretization in the three spatial directions, whith local Lax-Friedrichs interface fluxes and a specific treatment of the gravity

term improving the stability of the method (for a detailed description of the model, see Blaise et al. (submitted manuscript, 2015)). Given the large contrast between horizontal and vertical dynamics in atmospheric flows, the mesh is obtained by extruding over the vertical a horizontal unstructured mesh. The available time-integration schemes are fully explicit, fully implicit, as well as implicit/explicit (IMEX) Runge-Kutta methods. The IMEX scheme treats implicitly the fast acoustic waves, or alternatively their vertical component, in order to relax the CFL constraint on the time step while avoiding the need to solve a global nonlinear system (for details, see *Giraldo et al*. [2010]; Blaise et al. (submitted manuscript, 2015)).

Boundary conditions are weakly imposed by setting appropriate exterior values for the variables when computing the Lax-Friedrichs flux at a boundary edge [*Hesthaven and Warburton*, 2008]. No sponge layer was needed for any of the test cases presented here. No filtering or explicit diffusion has been used.

7.2. Three-Dimensional Global Transport

This test-case, designed by *Kent et al*. [2014] and referred to as the Hadley-like meridional circulation, is used to evaluate the advection scheme in both the vertical and horizontal directions. The domain is the global sphere of radius $R=6.37122 \cdot 10^6$ m, with a vertical coordinate $0 <= \alpha_3 <= H=12000$ m. A tracer q is deformed during the simulation. It is initialized as a vertical layer, given by

$$\begin{cases} \frac{1}{2}\left(1+\cos\left(\frac{2\pi\left(\alpha_3-\alpha_3^{\text{mean}}\right)}{\alpha_3^{\max}-\alpha_3^{\min}}\right)\right) & \text{if } \alpha_3^{\min} < \alpha_3 < \alpha_3^{\max}, \\ 0 & \text{otherwise,} \end{cases} \tag{25}$$

with $\alpha_3^{\min}=2000$ m, $\alpha_3^{\max}=5000$ m and $\alpha_3^{\text{mean}}=0.5(\alpha_3^{\min}+\alpha_3^{\max})$. The zonal, meridional and vertical velocity fields in the longitude-latitude space (λ, φ) read

$$u_\lambda = u_0 \cos(\varphi), \tag{26}$$

$$u_\varphi = -\frac{R w_0 \pi p_0}{K H R_d T_0 \rho} \cos(\varphi) \sin(K\varphi) \cos\left(\frac{\pi\alpha_3}{H}\right) \cos\left(\frac{\pi t}{\tau}\right) \tag{27}$$

$$u_3 = \frac{w_0 p_0}{K R_d T_0 \rho}\left(-2\sin(K\varphi)\sin(\varphi) + K\cos(\varphi)\cos(K\varphi)\right) sin\left(\frac{\pi\alpha_3}{H}\right) \cos\left(\frac{\pi t}{\tau}\right), \tag{28}$$

with $u_0=40$ ms^{-1}, $w_0=0.15$ ms^{-1}, $R_d = 287$ Jkg^{-1} K^{-1}, $T_0=300$ K, $p_0=10^5$ Pa and $K = 5$. The time-independent density is defined by

$$\rho = \frac{p_0}{R_d T_0} \exp\left(\frac{-\alpha_3 g}{R_d T_0}\right), \tag{29}$$

with $g = 9.80616$ ms^{-2}. The model is run for a complete period $\tau = 86400$ s (1 day), such that the final solution corresponds to the initial condition to which it can be compared in order to compute the error (Figure 5).

Simulations were performed using polynomial degrees P from 1 to 4, which are denoted $p1$, $p2$, $p3$ and $p4$. The coarsest simulations are characterized by an approximate resolution of 4° horizontally (resolution $\simeq \frac{360\Delta x}{2\pi RP}$) and 800 m vertically (resolution $\simeq \frac{\Delta x}{P}$). The finer meshes used for the convergence study are obtained by doubling successively this resolution in both directions simultaneously. A no-flux condition (wall) is imposed at the domain boundaries.

At an approximate resolution of 1°, the results are similar to those of *Kent et al*. [2014]. However, the loss of tracer at approximately 30° N and 30° S is much less pronounced and the solution seems closer to the analytical one (Figure 5). As a counterpart, oscillations around the constant zero value are generated as well as overshoots, which are typical of unfiltered high-order methods.

The convergence of the L_2 error on the tracer is shown in Figure 6. Despite increasing the polynomial order, the rate of convergence seems to be capped at a value of about 2.6. Such a behavior is due to the lack of regularity of the initial condition and can be explained by approximation theory. Because of the transition between a cosine and a constant zero value at the vertical coordinates $\alpha_3^{\min}$ and $\alpha_3^{\max}$ in (25), the initial solution is only C^1 continuous (i.e., its first-order derivatives are continuous but not the second-order ones). This initial condition is used as the analytical solution for $t = 24$ h. However, it is known that, for a C^1 analytical solution approximated by a finite element discretization, the maximum convergence rate guaranteed by

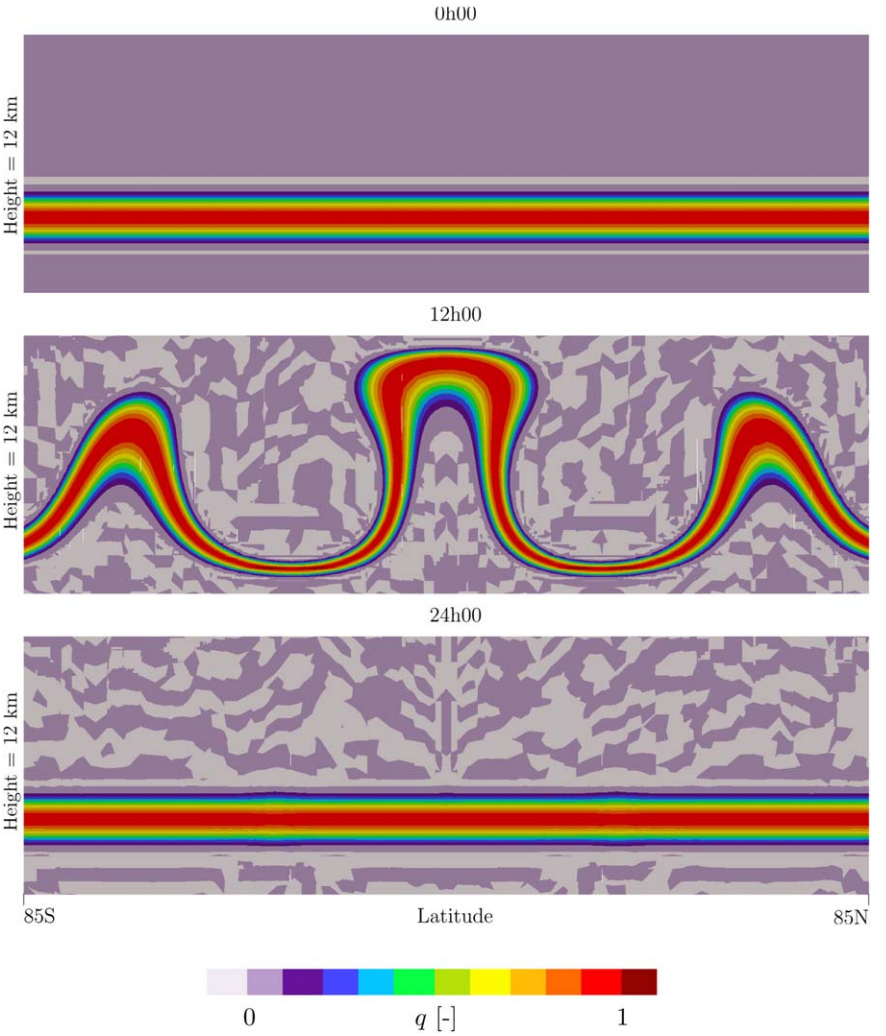

Figure 5. Three-dimensional global transport: latitude-height plots at $\lambda = 180^{\circ}$ of the tracer at time (top) $t = 0$, (middle) $t = 12$ h, and (bottom) $t = 24$ h. Simulation performed on meshes of third-order elements, with approximate horizontal and vertical resolutions of respectively 1° and 200 m. To facilitate comparisons, the color scale is the same as the one shown by *Kent et al*. [2014].

the method is 2 [e.g., *Rahman*, 2008; *Koren and Vuik*, 2009]. We observed a similar behavior on simplified two-dimensional advection test cases.

7.3. Three-Dimensional Gravity Waves on the Sphere

As a first validation of the complete set of equations, we resort to a configuration developed by *Baldauf et al*. [2014]: the propagation of three-dimensional gravity waves on the sphere.

This test case, for which an analytical solution is available, allows one to analyze the order of convergence of the scheme without relying upon high-resolution solutions obtained either by the tested model or a different one. It consists of a global atmospheric domain on the sphere in which gravity waves are triggered by an initial perturbation of the potential temperature in the form of a warm bubble. The waves then propagate around the planet (Figure 7).

The computational domain is a shell of depth 10,000 m around a planet of radius 50 times smaller than the Earth radius: $R = 63{,}71{,}229/50$ m. This planet rotates around its axis with an angular velocity 10 times higher that the Earth's angular velocity: $\boldsymbol{\omega} = \frac{10 \cdot 2\pi}{86164.04} \hat{\mathbf{e}}_3$ s^{-1}. The definition of the test case considers a gravitational acceleration $g = 9.80665$ m s^{-2} describing only the pure gravitational force due to the mass of the Earth;

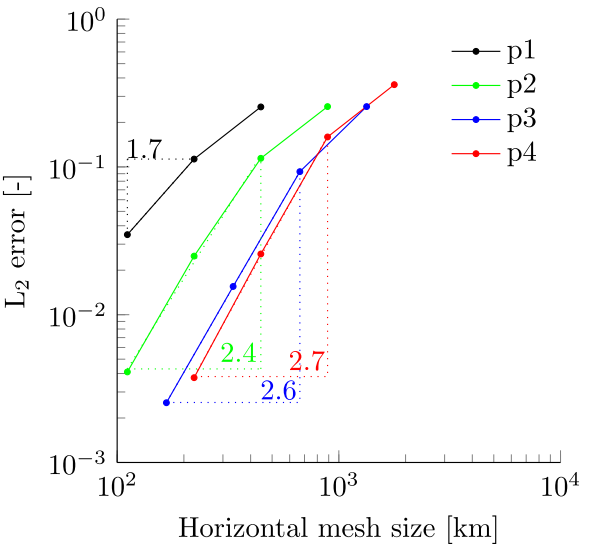

Figure 6. Three-dimensional global transport: spatial convergence of the L_2 error for the tracer at the end of the simulation, using spatial polynomial orders from 1 to 4.

while an additional term $(R+\alpha_3)\rho\boldsymbol{\omega}\times(\boldsymbol{\omega}\times\hat{\mathbf{g}}_3)$ is added to the right-hand side of the momentum equation (9b) to take into account the effect of the apparent centrifugal force.

The initial atmosphere is described by a stably stratified state perturbed by a warm bubble. The hydrostatic background state reads:

$$\bar{\rho}=\rho_0\exp(-\delta\alpha_3), \tag{30}$$

$$\bar{\theta}=T_0\exp(\delta\alpha_3)^{\frac{R_d}{c_p}}, \tag{31}$$

$$\bar{p}=p_0\exp(-\delta\alpha_3), \tag{32}$$

with $\rho_0=p_0\delta/g$ and $\delta=g/(R_dT_0)$. The background constant temperature T_0 is set to 250 K. According to *Baldauf et al.* [2014], the following constants are used: $R_d=287.05$ Jkg^{-1} K^{-1}, $c_p=1005$ Jkg^{-1} K^{-1}. The gravity waves are excited by an initial perturbation of the background state, corresponding to a warm bubble centered at the equator:

$$\rho'=\exp(-\delta\alpha_3/2)\rho_b, \tag{33}$$

$$T'=\exp(\delta\alpha_3/2)T_b, \tag{34}$$

$$p'=0, \tag{35}$$

with

$$\rho_b=-\frac{p_0T_b}{T_0^2R_d}, \tag{36}$$

$$T_b=\Delta T\exp(100(\sin(\gamma)-1))\sin\left(\frac{\pi\alpha_3}{H}\right), \tag{37}$$

where γ is the angular distance from the center of the bubble, which can be located anywhere at the equator. The temperature perturbation of the bubble ΔT is set to 0.01 K. The initial solution in terms of the model variable $(\rho\theta)'$ can be obtained using:

$$\overline{\rho\theta}=\bar{\rho}\,\bar{\theta}, \tag{38}$$

$$(\rho\theta)'=(\bar{\rho}+\rho')(T_0+T')\left(\frac{p_0}{\bar{p}}\right)^{\frac{R_d}{c_p}}-\overline{\rho\theta}. \tag{39}$$

A zonal flow, corresponding to a solid-body rotation around the planet axis $\mathbf{u}=-\boldsymbol{\omega}\times\hat{\mathbf{e}}_3$ is initially considered. This flow exacty compensates the rotation of the planet such that the advection, Coriolis and centrifugal terms for the background flow perfectly cancel in the momentum equation.

Unfortunately, the availability of an analytical solution is conditioned upon the use of the shallow-atmosphere approximation. While our modified stereographic transformation (1) naturally handles deep atmosphere effects, it is necessary to introduce the shallow-atmosphere approximation in the model to compare the results with the exact solution. This approximation is applied by replacing every $R+\alpha_3$ with R in the implementation of the differential operators.

The coarsest resolution mesh has horizontal and vertical element sizes of respectively 60 km and $\frac{10}{3}$ km. The finer meshes used for the convergence study are obtained by successively dividing the mesh size by $\sqrt{2}$. Free slip boundary conditions (i.e., zero normal velocity) are enforced at the lower and upper boundaries. An explicit Runge-Kutta time disretization of order 2 is used, with the largest time step (i.e., used for the $p1$ simulation on the coarsest mesh) being 1.05 s.

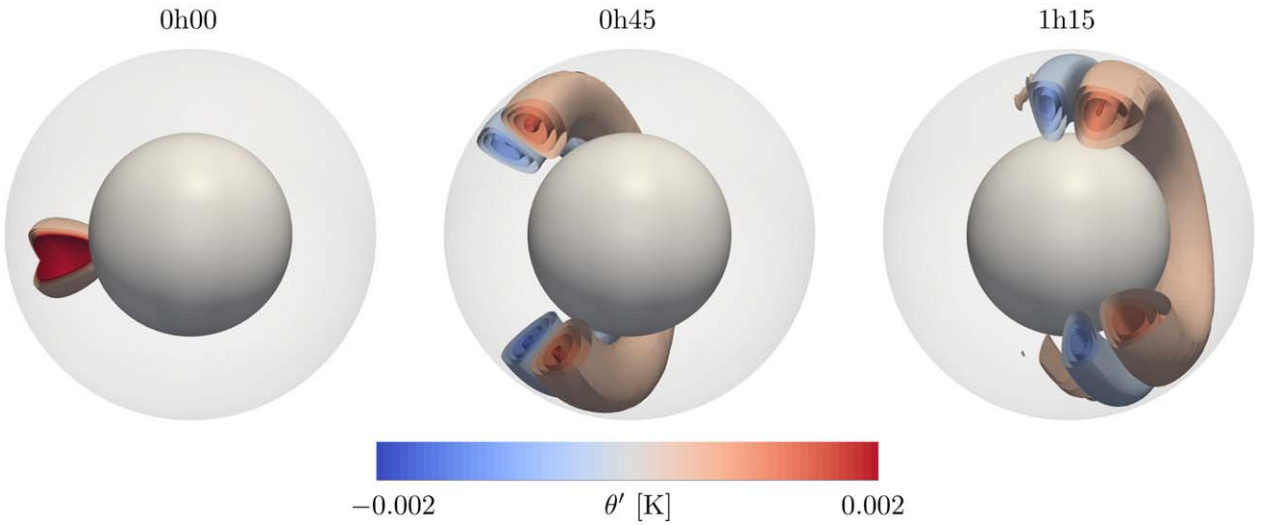

Figure 7. Propagation of gravity waves on the sphere: potential temperature perturbation in several phases. The simulation was performed using third-order polynomials on a mesh of 30 km horizontal resolution and 6 vertical layers. For visualization purposes, the solution is clipped to visualize the different contours; and the atmosphere depth is stretched by a factor of 10.

The results obtained from the model exhibit a convergence rate in good agreement with the theoretical expectations (Figure 8). It is possible to verify that the error is not specifically concentrated along the seam between the northern and southern hemispheres. Figure 9 shows the model results and associated discretization error for the *p*3 simulation using the initial mesh with two levels of refinement (i.e., horizontal and vertical mesh resolutions of 30 km and $\frac{5}{3}$ km). The error is well distributed inside the domain and not significantly higher along the seam (green line).

7.4. Baroclinic Instability

After a validation on quite simple test cases, the model is tested on a more complex and realistic benchmark, developed by *Jablonowski and Williamson* [2006]. Widely used for models validations and intercomparisons [e.g., *Park et al.*, 2013; *Lauritzen et al.*, 2010], the test case consists in the evolution of a baroclinic instability in the northern hemisphere. Such an instability is the main mechanism responsible for the formation of cyclones and anticyclones characteristic of the weather in midlatitudes.

The hydrostatic background temperature, averaged over the horizontal reads:

$$\bar{T} = T_0 \eta^{\frac{R_d \tau}{g}} \qquad \text{for } \eta_s \geq \eta \geq \eta_t, \tag{40}$$

$$\bar{T} = T_0 \eta^{\frac{R_d \tau}{g}} + \Delta T (\eta_t - \eta)^5 \qquad \text{for } \eta_{top} \geq \eta, \tag{41}$$

in which $R_d = 287.04$ Jkg^{-1} K^{-1} and $\eta = \frac{p}{p_0}$ is the pressure-based vertical coordinate. The surface, tropopause and upper boundary levels are respectively $\eta_s = 1$, $\eta_t = 0.2$ and $\eta_{top} = 0.1$. The temperature lapse rate τ is 0.005 Km^{-1}. The gravitational acceleration is set to $g = 9.80616$ ms^{-2}, while the horizontal-mean temperature at the surface is $T_0 = 288$ K and $\Delta T = 4.8 \cdot 10^5$ K. A horizontal variation T', expressed in the longitude-latitude space (λ, φ), is added to this background state:

$$T' = \frac{3}{4}\frac{\eta \pi U_0}{R_d} \sin(\eta_v) \sqrt{\cos(\eta_v)} \left[\left(-2\sin^6(\varphi) \left(\cos^2(\varphi) + \frac{1}{3} \right) + \frac{10}{63} \right) 2U_0 \cos^{\frac{3}{2}}(\eta_v) + \left(\frac{8}{5}\cos^3(\varphi) \left(\sin^2\varphi + \frac{2}{3} \right) - \frac{\pi}{4} \right) a\boldsymbol{\omega} \cdot \hat{\mathbf{e}}_3 \right], \tag{42}$$

where the Earth's angular velocity is $\boldsymbol{\omega} = 7.29212 \cdot 10^{-5}\, \hat{\mathbf{e}}_3$ s^{-1}.

The temperature $\mathrm{T} = \bar{T} + T'$ can be converted into the model variables using

$$\theta = T \frac{p_0^{\frac{R_d}{c_p}}}{p}, \tag{43}$$

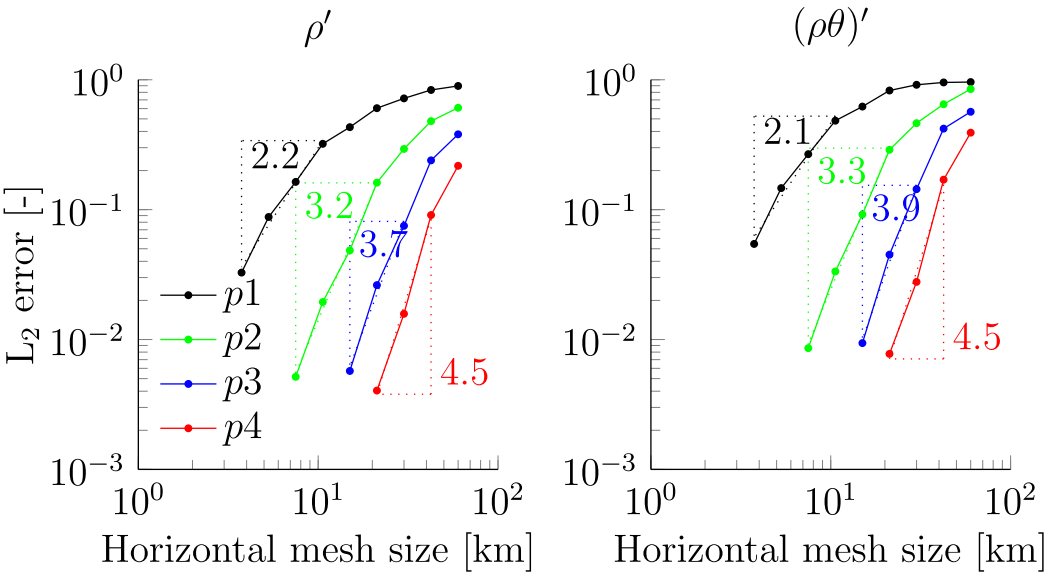

Figure 8. Propagation of gravity waves on the sphere: spatial convergence of the L_2 error after 75 min for $\rho\prime$ and $(\rho\theta)\prime$, using spatial polynomial orders from 1 to 4.

$$\rho = \left(\frac{p}{p_0}\right)^{\frac{c_v}{c_p}} \frac{p_0}{\theta R_d}, \tag{44}$$

with $c_p = 1004.64$ Jkg^{-1} K^{-1} and $p = \eta p_0$.

An initial zonal wind u_λ is defined, characterized by a background value of amplitude $U_0 = 35$ ms^{-1} to which a perturbation of magnitude $u_p = 1$ ms^{-1} is added, centered around $(\lambda_c = \frac{\pi}{9}, \varphi_c = \frac{2\pi}{9})$:

$$u_\lambda = U_0 \cos^{\frac{3}{2}}(\eta_v) \sin^2(2\varphi) + u_p \exp\left(-\left(\frac{10r}{R}\right)^2\right), \tag{45}$$

with $r = R\arccos\left(\sin(\varphi_c)\sin(\varphi) + \cos(\varphi_c)\cos(\varphi)\cos(\lambda - \lambda_c)\right)$ and the Earth radius $R = 6{,}371{,}229$ m.

The initial state is written in terms of the η pressure-based vertical coordinate, while the model is based upon height coordinates. Then, an additional equation is needed to compute η from the height α_3 and close the system. The missing link is provided by the geopotential $\Phi = g\alpha_3$, which is also split into a horizontal-mean value and a horizontal variation $\Phi = \bar{\Phi} + \Phi'$. The horizontally averaged geopotential reads:

$$\bar{\Phi} = \frac{T_0 g}{\tau}\left(1 - \eta^{\frac{R_d \tau}{g}}\right) \qquad \text{for } \eta_s \geq \eta \geq \eta_t, \tag{46}$$

$$\begin{aligned} \bar{\Phi} &= \frac{T_0 g}{\tau}\left(1 - \eta^{\frac{R_d \tau}{g}}\right) \\ &- R_d \Delta T\left[\left(\ln\left(\frac{\eta}{\eta_t}\right) + \frac{137}{60}\right)\eta_t^5 - 5\eta_t^4\eta + 5\eta_t^3\eta^2 - \frac{10}{3}\eta_t^2\eta^3 + \frac{5}{4}\eta_t\eta^4 - \frac{1}{5}\eta^5\right] \qquad \text{for } \eta_{top} \geq \eta, \end{aligned} \tag{47}$$

while its horizontal variation is:

$$\Phi' = U_0 \cos^{\frac{3}{2}}(\eta_v)\left[\left(-2\sin^6(\varphi)\left(\cos^2(\varphi) + \frac{1}{3}\right) + \frac{10}{63}\right)U_0 \cos^{\frac{3}{2}}(\eta_v) + \left(\frac{8}{5}\cos^3(\varphi)\left(\sin^2\varphi + \frac{2}{3}\right) - \frac{\pi}{4}\right)R\boldsymbol{\omega}\cdot\hat{\mathbf{e}}_3\right]. \tag{48}$$

The level pressure coordinate η can then be obtained from the height coordinate α_3 by iterating over equations (46–48) until the geopotential corresponding to the height α_3 is attained (for details, see *Jablonowski and Williamson* [2006, Appendix]).

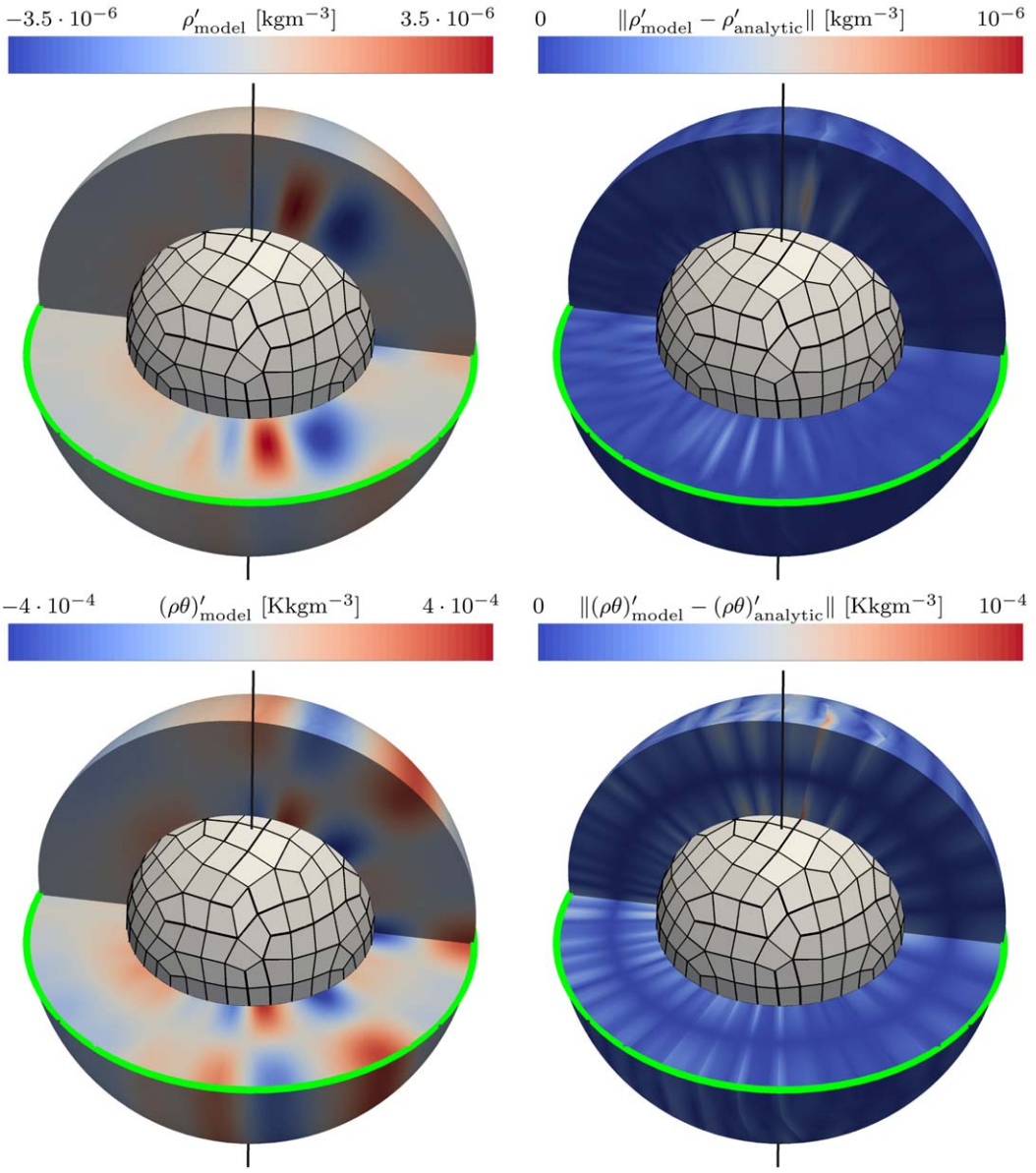

Figure 9. Propagation of gravity waves on the sphere: (left) model solution for $\rho\prime$ and $(\rho\theta)\prime$ after 75 min, and (right) corresponding model error. The simulation was performed using third-order polynomials on a mesh of 30 km horizontal resolution and 6 vertical layers. The green circle represents the equator line. For visualization purposes, the solution is clipped to visualize the different contours; and the atmosphere depth is stretched by a factor of 10.

The traditional approximation is considered for the Coriolis force:

$$-2\rho\boldsymbol{\omega}\times\mathbf{u} \simeq 2\rho\sin(\varphi)\boldsymbol{\omega}\cdot\hat{\mathbf{e}}_3\left(u_1^{\alpha}\hat{\mathbf{g}}_1 - u_2^{\alpha}\hat{\mathbf{g}}_2\right). \tag{49}$$

Free slip conditions are used at the bottom boundary, while the initial background state is enforced at the upper limit of the domain, which is defined by $\eta = 0.1$.

Four simulations have been performed using third-order elements, with horizontal mesh sizes Δx of 333, 667, 1000, and 1333 km, corresponding respectively to approximate resolutions of 1, 2, 3 and 4° at the equator (resolution $\simeq \frac{360\Delta x}{2\pi RP}$). The atmosphere depth is discretized using 9 layers of elements, placed at equidistant η coordinates. This number of layers corresponds approximately to the 26 levels used by the different models whose results are displayed in the intercomparison study from *Jablonowski and Williamson* [2006], considering spectral transform, finite volume, semi-lagrangian and finite difference models. Given

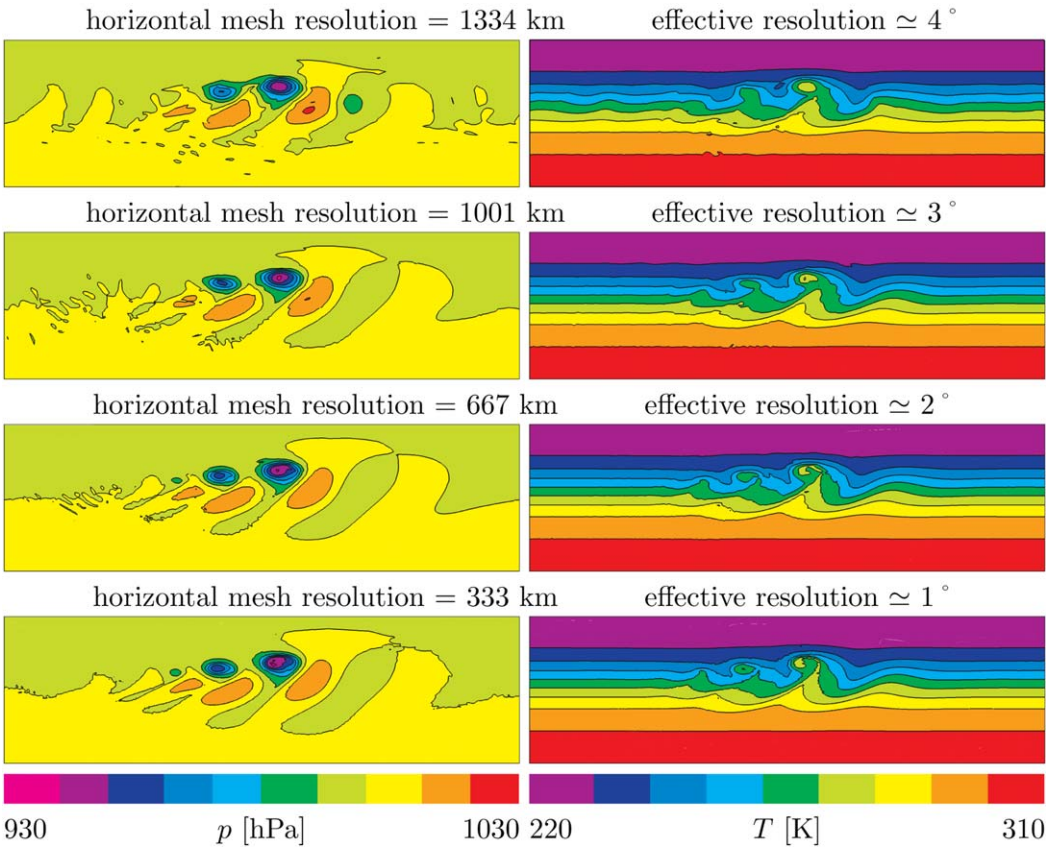

Figure 10. Baroclinic instability: (left) surface pressure and (right) temperature at the pressure level $p = 850$ hPa at day 9. Simulations performed on meshes of third-order elements, made up of nine layers with increasing horizontal resolution. To facilitate comparisons, the colors, scales and contour intervals are the same as those shown by *Jablonowski and Williamson* [2006]. For the same reason, only a part of the domain is displayed, covering the longitude-latitude interval $[45^\circ, 360^\circ] \times [0^\circ, 90^\circ]$.

the large aspect ratio, an IMEX time discretization with vertical linear terms implicit has been used (for details see e.g., *Giraldo et al.* [2010]), with time steps ranging from 57.5 s for the coarsest mesh to 12.9 s for the 1° simulation.

Simulation results at day 9 are similar to the results presented by *Jablonowski and Williamson* [2006], displaying closed cells in the surface pressure field (Figure 10, left) and wave breaking in the temperature field (Figure 10, right). However, at a similar resolution in terms of grid spacing, the simulations appear to be more accurate with the discontinuous Galerkin model. Indeed, the pressure and temperature fields obtained from the DG model at the coarsest resolution (4°) are much more resolved than the results on similar resolutions provided by the models tested by *Jablonowski and Williamson* [2006]. The third and smallest closed cell in the surface pressure fields (the leftmost one) appears at a resolution of 2°, while the spectral eulerian dynamical core or the finite volume dynamical core from *Jablonowski and Williamson* [2006] were not able to reproduce that closed cell with a grid size higher than 0.5°. The 2° DG simulation is almost resolved, and a resolution enhancement to 1° barely improves the results. As a comparison, the models presented by *Jablonowski and Williamson* [2006] seem to be converged at a resolution of 0.5°.

Obviously, those are approximate resolutions, and it is difficult to compare resolutions associated with simulations carried out using different methods. For the same reason, the resolution is not an indicator of the computational cost. However, those results confirm the good behavior and low numerical dissipation of the discontinuous Galerkin method in the case of atmospheric simulations.

Another advantage of the discontinuous Galerkin method, which is also a characteristic of the finite volume method, is its ability to rely upon variable resolution unstructured meshes. Such grids allow for increasing the resolution exactly where needed, in order to use efficiently the computational resources. It is of great

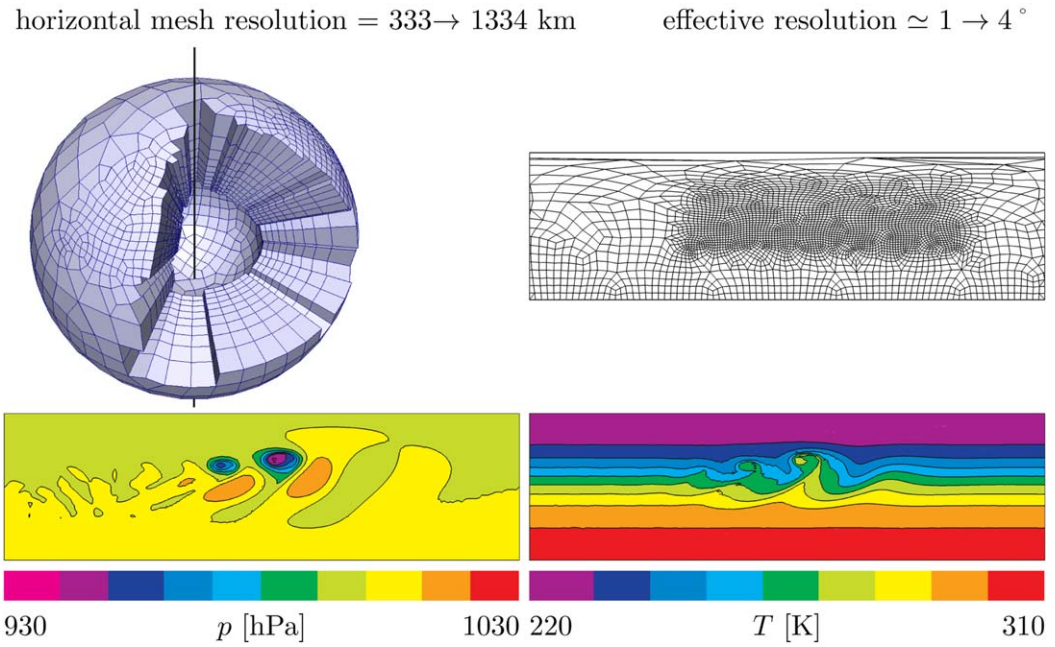

Figure 11. Baroclinic instability. (top) unstructured computational grid with variable horizontal resolution used for the simulation. Three-dimensional mesh on the sphere, from which elements have been removed to display the (left) vertical structure, and (right) two-dimensional horizontal slice in the longitude-latitude space, in a subset of the domain covering the interval [45°, 360°] × [0°, 90°]. (bottom) (left) surface pressure and (right) temperature at the pressure level $p = 850$ hPa at day 9. To facilitate comparisons, the colors, scales, contour intervals and part of the domain displayed are the same as those shown by *Jablonowski and Williamson* [2006].

interest for regional modeling: a higher resolution is considered in the region of interest, while the rest of the domain is discretized at a lower resolution. Doing that, the simulation of local processes is considered in a global context, taking into account the interactions between the different scales.

The method presented in this study to solve the equations on the sphere is independent of the choice of the grid, such that unstructured meshes can be used to simulate the baroclinic instability test case by refining locally the mesh in the region surrounding the instability. To do so, we consider the finest resolution (1°) in the region of interest $(\lambda, \varphi) \in [140^\circ, 310^\circ] \times [30^\circ, 75^\circ]$. Around this region, in a transition zone of width 10°, the grid size varies linearly to attain the coarsest resolution (4°), which is kept constant in the rest of the domain (Figure 11).

The numerical results are quite smooth, and no spurious reflexion or oscillation is produced in the transition zone between the high and the low-resolution regions. In the high-resolution region, the results are accurately reproduced, and similar to those obtained from the homogeneous grid simulation at the same resolution. In the coarse resolution region, results are obviously less accurate. As an example, the smallest closed cell, which was visible for the constant high-resolution run, does not appear on the variable resolution mesh simulation because of its location outside of the refined region. Using seven times less elements, the simulation with variable resolution produces the expected results, very similar to those obtained resorting to a high constant resolution in the region of interest, and comparable to those based upon a low resolution grid outside of that region.

7.5. Baroclinic Instability With Deep-Atmosphere Effects

This last test case aims at validating the model ability to simulate deep-atmosphere effects. Recently designed by *Ullrich et al*. [2013] and carried out by *Wood et al*. [2014], it is an analogous baroclinic wave test case as the one proposed by *Jablonowski and Williamson* [2006], but is appropriate for shallow and deep-atmosphere dynamical cores.

It consists in an initial basic state expressed in longitude-latitude coordinates (λ, φ), to which a perturbation is added in the zonal and meridional wind components to trigger the baroclinic wave. The test case can be

configured in shallow or deep-atmosphere modes. The initial temperature for the deep-atmosphere configuration reads

$$T=\left(\frac{R}{r}\right)^2\left(\tilde{\tau}_1-\tilde{\tau}_2\left(\left(\frac{r}{R}\cos\varphi\right)^k-\left(\frac{k}{k+2}\right)\left(\frac{r}{R}\cos\varphi\right)^{k+2}\right)\right)^{-1}, \tag{50}$$

where $k=3$ and $r=R+\alpha_3$ is the distance from the center of the Earth, whose radius $R=\frac{6371229}{20}$ m is reduced in order to increase the deep-atmosphere effects. The arbitrary functions $\tilde{\tau}_1$ and $\tilde{\tau}_2$ read

$$\tilde{\tau}_1(r)=A\frac{\Gamma}{T_0}\exp\left(\frac{\Gamma}{T_0}(r-R)\right)+B\left(1-2\left(\frac{r-R}{bH}\right)^2\right)\exp\left(-\left(\frac{r-R}{bH}\right)^2\right), \tag{51}$$

$$\tilde{\tau}_2(r)=C\left(1-2\left(\frac{r-R}{bH}\right)^2\right)\exp\left(-\left(\frac{r-R}{bH}\right)^2\right), \tag{52}$$

with $A=\frac{1}{\Gamma}$, $B=\frac{T_0-T_0^p}{T_0T_0^p}$ and $C=\left(\frac{k+2}{2}\right)\left(\frac{T_0^E-T_0^p}{T_0^ET_0^p}\right)$. Constant parameters are set to $b=2$, $\Gamma=0.005$ Km^{-1}, $T_0^E=310$ K, $T_0^p=240$ K and $T_0=275$ K. The basic state for the initial pressure is defined as

$$p=p_0\exp\left(-\frac{g}{R_d}\int_R^r\tilde{\tau}_1(r')\mathrm{d}r'+\frac{g}{R_d}\int_R^r\tilde{\tau}_2(r')\mathrm{d}r'\left(\left(\frac{r}{R}\cos\varphi\right)^k-\frac{k}{k+2}\left(\frac{r}{R}\cos\varphi\right)^{k+2}\right)\right), \tag{53}$$

in which $R_d=287$ Jkg^{-1} K^{-1}, $g=9.80616$ ms^{-2} and $p_0=10^5$ Pa. The integrals are computed from (51) and (52) to obtain

$$\int_R^r\tilde{\tau}_1(r')\mathrm{d}r'=A\left(\exp\left(\frac{\Gamma}{T_0}(r-R)\right)-1\right)+B(r-R)\exp\left(-\left(\frac{r-R}{bH}\right)^2\right), \tag{54}$$

$$\int_R^r\tilde{\tau}_2(r')\mathrm{d}r'=C(r-R)\exp\left(-\left(\frac{r-R}{bH}\right)^2\right). \tag{55}$$

Pressure and temperature fields can be converted into model variables using (43) with $c_p=1004.5$ Jkg^{-1} K^{-1} and $c_v=717.5$ Jkg^{-1} K^{-1}. Only the zonal component of the wind field u_λ is nonzero for the basic state, given by

$$u_\lambda^{\text{basic}}=-\omega r\cos\varphi+\sqrt{\omega^2r^2\cos^2\varphi+r\cos\varphi U}, \tag{56}$$

with $\omega=7.29212\cdot10^{-5}$ s^{-1} and

$$U=\frac{g}{R}kT\int_R^r\tilde{\tau}_2(r')\mathrm{d}r'\left(\left(\frac{r}{R}\cos\varphi\right)^{k-1}-\left(\frac{r}{R}\cos\varphi\right)^{k+1}\right). \tag{57}$$

A perturbation is then added to this basic state such that

$$u_\lambda=u_\lambda^{\text{basic}}-\frac{16V_p}{3\sqrt{3}}\Psi\cos^3\left(\frac{\pi d}{2d_0}\right)\sin\left(\frac{\pi d}{2d_0}\right)\frac{-\sin\varphi_c\cos\varphi+\cos\varphi_c\sin\varphi\cos(\lambda-\lambda_c)}{\sin(d/R)}, \tag{58}$$

$$u_\varphi=\frac{16V_p}{3\sqrt{3}}\Psi\cos^3\left(\frac{\pi d}{2d_0}\right)\sin\left(\frac{\pi d}{2d_0}\right)\frac{\cos\varphi_c\sin(\lambda-\lambda_c)}{\sin(d/R)}, \tag{59}$$

with $(\varphi_c,\lambda_c)=(\pi/9,\pi/9)$, $V_p=1$ ms^{-1}, $d_o=R/6$ and

$$d=R\cos^{-1}(\sin\varphi_c\sin\varphi+\cos\varphi_c\cos\varphi\cos(\lambda-\lambda_c)). \tag{60}$$

The vertical taper function Ψ associated with the velocity perturbation reads

$$\begin{cases}\Psi=1-3\left(\frac{z}{z_t}\right)^2+2\left(\frac{z}{z_t}\right)^3 & \text{if } 0\le\alpha_3\le\alpha_3^t,\\ 0 & \text{elsewhere,}\end{cases} \tag{61}$$

with $\alpha_3^t=1.5\cdot10^4$ m. The analogous shallow-atmosphere initial state is obtained by setting any occurence of $\frac{R}{r}$ or $\frac{r}{R}$ equal to unity in (50), (53), and (57), as well as replacing r by R in (56).

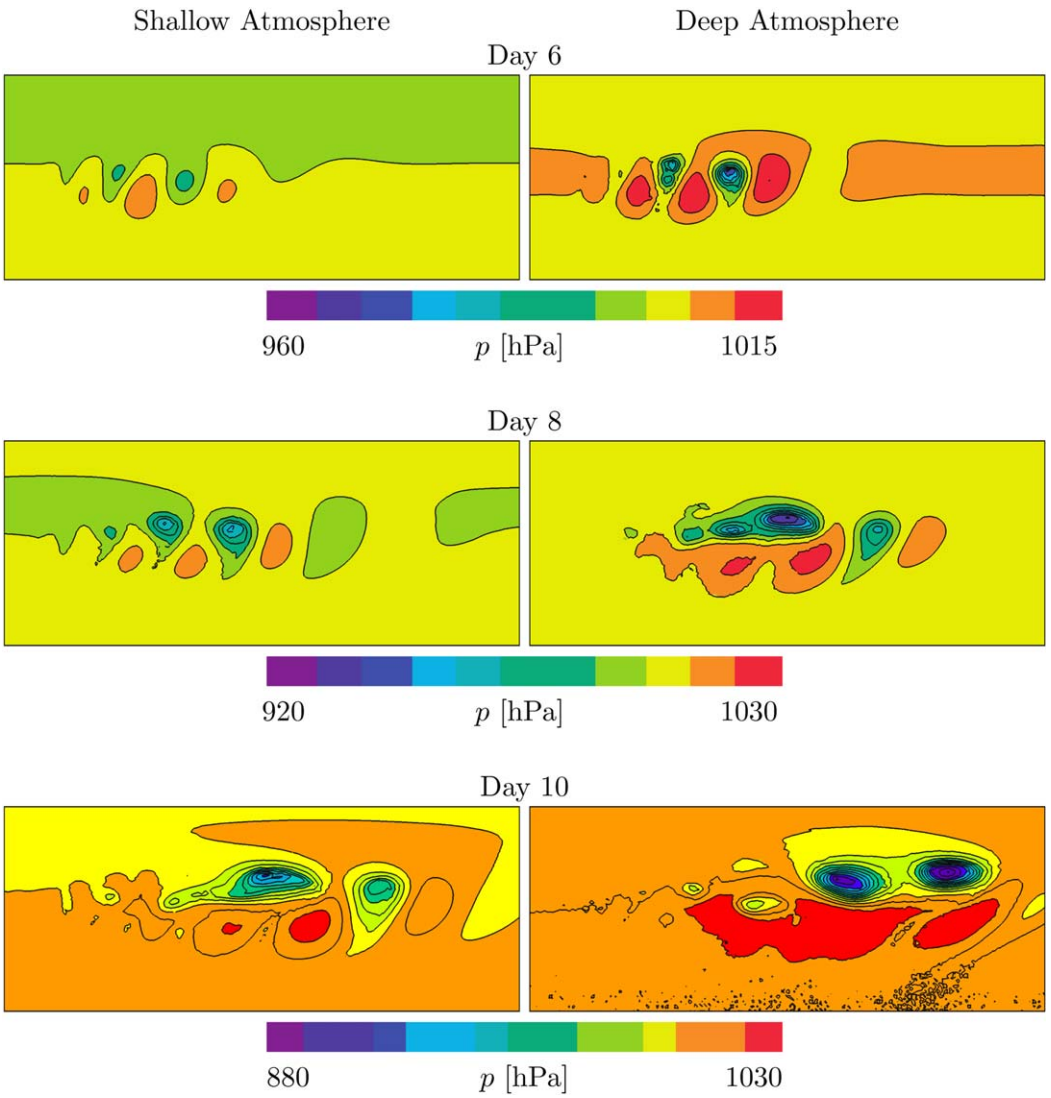

Figure 12. Baroclinic instability with deep-atmosphere effects: surface pressure at days 6, 8, and 10 for the shallow-atmosphere configuration (left) and deep-atmosphere configuration (right). Simulations performed on meshes of third-order elements, made up of 10 layers and a horizontal elements size of 333/20 km. The resulting approximate resolution is 1°. To facilitate comparisons, the colors, scales and contour intervals are the same as those shown by *Ullrich et al*. [2013]. For the same reason, only a part of the domain is displayed, covering the longitude-latitude interval $[0^\circ, 240^\circ] \times [0^\circ, 90^\circ]$.

Free slip conditions are enforced at the bottom and upper boundaries. The complete coriolis term of (9) is considered, without recourse to the traditional approximation. Two simulations have been performed, in shallow and deep-atmosphere configurations. They have been performed using third-order elements, with a horizontal mesh size Δx of 333 km, corresponding to an approximate resolution of 1° at the equator. The atmosphere depth is discretized using 10 layers of elements. Similarly to *Ullrich et al*. [2013], the height of the nth interface between two levels is set to

$$\alpha_3^n = \alpha_3^{\text{top}} \frac{\sqrt{\mu(n/30)^2+1}-1}{\sqrt{\mu+1}-1}, \tag{62}$$

with the model top $\alpha_3^{\text{top}} = 3 \cdot 10^4$ m and $\mu = 15$. Given the large aspect ratio, an IMEX time discretization with vertical linear terms implicit has been used, with a scaled time step of 13.8 s.

The surface pressure fields resulting from the simulations (Figure 12) exhibit a structure similar to those of *Ullrich et al*. [2013] and *Wood et al*. [2014]: the pressure systems are at the same location and of comparable

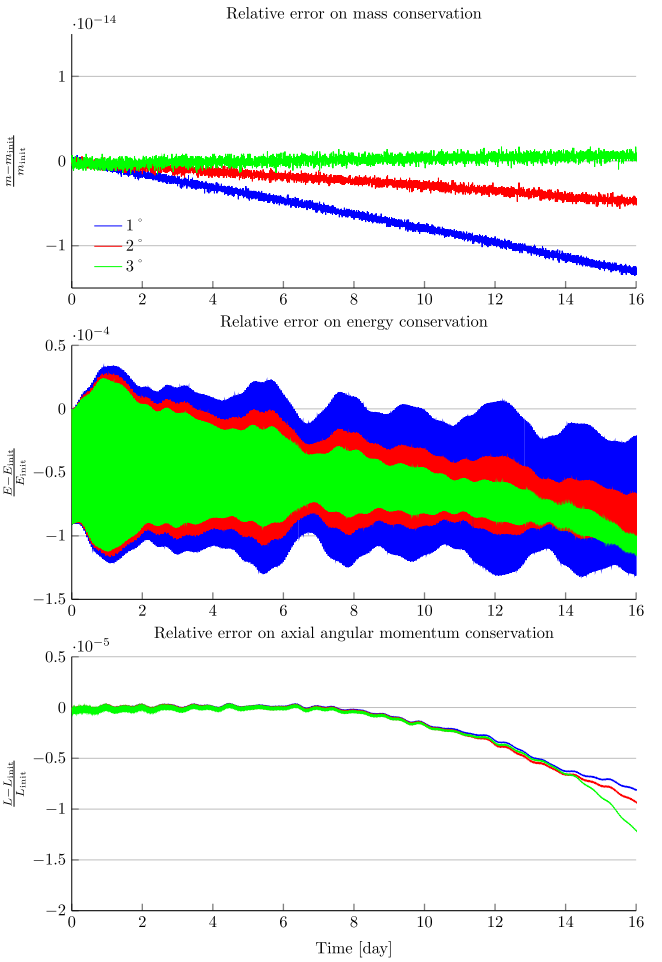

Figure 13. Baroclinic instability with deep-atmosphere effects: error in mass conservation, total energy and axial angular momentum during the whole simulation. Simulations performed on meshes of third-order elements, made up of 10 layers and horizontal elements sizes of 333/20, 667/20, and 1000/20 km. The resulting approximate resolutions are 1, 2 and 3°.

strength. For a similar resolution, while the discontinuous Galerkin model and the semi-Lagrangian model from *Wood et al.* [2014] exhibit three closed cells at day 8 for the shallow-atmosphere version, the MCore model of *Ullrich et al.* [2013] only has two, suggesting a lower accuracy. The differences between shallow and deep-atmosphere simulations are pronounced, with a more rapid intensification of the wave and stronger pressure systems for the deep-atmosphere version.

The conservation of the total mass of the system (i.e., the integral of ρ over the physical domain) is a critical aspect for geophysical simulations. To verify that the discretization preserves mass conservation, simulations of the baroclinic instability with deep-atmosphere effects have been performed on three meshes made up of 10 layers and horizontal elements sizes of 333/20, 667/20, and 1000/20 km. Third-order polynomials are resorted to, resulting in approximate resolutions of 1, 2 and 3°. As can be seen on Figure 13, the model is able to conserve mass up to the machine precision level for each tested resolution, thanks to the discontinuous Galerkin discretization and the careful handling of the equatorial seam. The error is slightly higher at finer resolutions, probably due to the higher number of operations increasing the accumulation of roundoff errors.

The total mass, based upon a linear invariant, can be exactly conserved. However, this is not the case for the total energy and angular momentum, whose errors in conservation are also displayed in Figure 13. The total energy of the system is computed as the integral over the whole domain of ρe, where $e = c_V T + \frac{\mathbf{u}\cdot\mathbf{u}}{2} + g\alpha_3$ is the sum of the internal, kinetic and potential specific energies. The total axial angular momentum L is the

integral over the domain of ρI with $I=\rho\sqrt{x_1^2+x_2^2}(\omega\sqrt{x_1^2+x_2^2}+u_\lambda)$, which includes the effect of the rotation of the Earth in addition to the relative velocity of the air mass. The overall pattern shows a slight decay of energy as long as the time increases. As expected, the loss of energy is reduced as the resolution is improved. However, the time series exhibit oscillations, whose amplitude decreases with time, especially at the lower resolutions. Those oscillations are likely to be connected with an adjustement of the initial condition projected into the discrete space. The angular momentum behaves as expected: it decreases with time, at a higher rate for low resolution simulations. When the instability develops at the end of the simulation, the more complex dynamics results in a faster decay of energy and angular momentum.

8. Conclusions

A method to solve the three-dimensional compressible Navier-Stokes equation on the sphere has been proposed, based on a stereographic projection with a high-order mapping of the elements from the stereographic space to the sphere. The projection is slightly modified, in order to take into account the domain depth without introducing any approximation about the aspect ratio.

In a discontinuous Galerkin framework, the elements alongside the equator are exactly represented using a nonpolynomial transformation, in order to avoid the numerical issues associated with the seam joining the northern and southern hemispheres.

The resulting model has been validated on idealized three-dimensional atmospheric test cases on the sphere, demonstrating the applicability of the method and the good convergence properties of the spatial discretization, as well as the mass conservation. Error distributions computed for the different test cases have shown that the seam is not the source of any significant discretization error, despite a nonexact numerical integration.

The baroclinic instability test case was used to assess the method in the presence of more complex flows. Those simulations confirmed the good behavior of the model in terms of accuracy and low numerical dissipation. Comparisons with existing models suggest that the proposed implementation is able to reproduce the main characteristics of the flow, even at lower resolutions. Simulations resulting from an analogous benchmark, including a deep-atmosphere configuration, confirmed the ability of the method to handle deep-atmosphere effects.

The method allows for the use of any type of unstructured grid. Simulation on such grids demonstrate the advantages of using variable resolution discretizations, by reducing substantially the number of elements while producing accurate results in the region of interest. Such an approach would be of great interest to improve regional models. However, other model components have to be improved for efficient multiscale simulations, such as resolution-aware parametrizations of unresolved physics or multirate temporal discretizations.

Appendix A: Complete Expression of the Equations in Stereographic Coordinates

In section 4, the continuous equations are presented in vector form (9a), and each term involving a differential operator has been expressed in the stereographic system of coordinates. In this appendix, those developments are gathered to write the complete continuous equations in stereographic coordinates.

Introducing (12) in the vector form of the continuity equation (9a) leads to its expression in terms of components in the stereographic basis:

$$\frac{\partial\rho'}{\partial t}+\frac{1}{J}\frac{\partial(\rho u_1)}{\partial\alpha_1}+\frac{1}{J}\frac{\partial(\rho u_2)}{\partial\alpha_2}+\frac{\partial(\rho u_3)}{\partial\alpha_3}+\frac{1}{R+\alpha_3}\left(2\rho u_3-\frac{\alpha_1\rho u_1+\alpha_2\rho u_2}{2R}\right)=0. \tag{A1}$$

The momentum equation is obtained similarly by introducing the development in stereographic coordinates of the advection (13), pressure (14) and diffusion (15) terms into its vector form (9b):

$$
\begin{aligned}
&\frac{\partial}{\partial t}\begin{pmatrix}\rho u_1\\ \rho u_2\\ \rho u_3\end{pmatrix}+\frac{1}{J}\frac{\partial}{\partial \alpha_1}\begin{pmatrix}\rho u_1^2\\ \rho u_1u_2\\ \rho u_1u_3\end{pmatrix}+\frac{1}{J}\frac{\partial}{\partial \alpha_2}\begin{pmatrix}\rho u_1u_1\\ \rho u_2^2\\ \rho u_2u_3\end{pmatrix}+\frac{\partial}{\partial \alpha_3}\begin{pmatrix}\rho u_1u_3\\ \rho u_2u_3\\ \rho u_3^2\end{pmatrix}\\
&+\begin{pmatrix}\frac{1}{J}\frac{\partial p'}{\partial \alpha_1}\\ \frac{1}{J}\frac{\partial p'}{\partial \alpha_2}\\ \frac{\partial p'}{\partial \alpha_3}\end{pmatrix}-\begin{pmatrix}\frac{1}{J^2}\frac{\partial\left(\rho\kappa_h\frac{\partial}{\partial \alpha_1}\right)}{\partial \alpha_1}+\frac{1}{J^2}\frac{\partial\left(\rho\kappa_h\frac{\partial}{\partial \alpha_2}\right)}{\partial \alpha_2}+\frac{\partial\left(\rho\kappa_v\frac{\partial}{\partial \alpha_3}\right)}{\partial \alpha_3}\end{pmatrix}\begin{pmatrix}u_1\\ u_2\\ u_3\end{pmatrix}\\
&+\frac{\rho}{R+\alpha_3}\begin{pmatrix}3u_1u_3-\frac{u_1}{2R}(\alpha_1u_1+2\alpha_2u_2)+\frac{\alpha_1u_2^2}{2R}-2\kappa_v\frac{\partial u_1}{\partial \alpha_3}+\frac{\kappa_hu_1}{R+\alpha_3}\left(1+\frac{\alpha_1^2+\alpha_2^2}{4R^2}\right)\\ 3u_2u_3-\frac{u_2}{2R}(\alpha_2u_2+2\alpha_1u_1)+\frac{\alpha_2u_1^2}{2R}-2\kappa_v\frac{\partial u_2}{\partial \alpha_3}+\frac{\kappa_hu_2}{R+\alpha_3}\left(1+\frac{\alpha_1^2+\alpha_2^2}{4R^2}\right)\\ 2u_3^2-u_1^2-u_2^2-\frac{u_3}{2R}(\alpha_1u_1+\alpha_2u_2)-2\kappa_v\frac{\partial u_3}{\partial \alpha_3}-\frac{1}{R+\alpha_3}\left(\frac{\kappa_h}{R}(\alpha_1u_1+\alpha_2u_2)-2\kappa_hu_3\right)\end{pmatrix}\\
&-\frac{1}{J(R+\alpha_3)}\begin{pmatrix}\frac{\partial(\rho\kappa_hu_3)}{\partial \alpha_1}+\rho\kappa_h\frac{\partial u_3}{\partial \alpha_1}+\frac{u_2}{2R}\left(\alpha_2\frac{\partial(\rho\kappa_h)}{\partial \alpha_1}-\alpha_1\frac{\partial(\rho\kappa_h)}{\partial \alpha_2}\right)+\frac{1}{R}\left(\alpha_1\frac{\partial(u_2\rho\kappa_h)}{\partial \alpha_2}-\alpha_2\frac{\partial(u_2\rho\kappa_h)}{\partial \alpha_1}\right)\\ \frac{\partial(\rho\kappa_hu_3)}{\partial \alpha_2}+\rho\kappa_h\frac{\partial u_3}{\partial \alpha_2}+\frac{u_1}{2R}\left(\alpha_1\frac{\partial(\rho\kappa_h)}{\partial \alpha_2}-\alpha_2\frac{\partial(\rho\kappa_h)}{\partial \alpha_1}\right)+\frac{1}{R}\left(\alpha_2\frac{\partial(u_1\rho\kappa_h)}{\partial \alpha_1}-\alpha_1\frac{\partial(u_1\rho\kappa_h)}{\partial \alpha_2}\right)\\ -\frac{\partial(\rho\kappa_hu_1)}{\partial \alpha_1}-\frac{\partial(\rho\kappa_hu_2)}{\partial \alpha_2}-\rho\kappa_h\left(\frac{\partial u_1}{\partial \alpha_1}+\frac{\partial u_2}{\partial \alpha_2}\right)\end{pmatrix}\\
&+\rho' g\hat{\mathbf{g}}_3+2\rho\boldsymbol{\omega}\times\mathbf{u}=0.
\end{aligned}
\tag{A2}
$$

Finally, the potential temperature equation in vector form (9c) can be rewritten with its components expressed in the stereographic basis using (16) and (17):

$$
\begin{aligned}
&\frac{\partial(\rho\theta)'}{\partial t}+\frac{1}{J}\frac{\partial(\rho\theta u_1)}{\partial \alpha_1}+\frac{1}{J}\frac{\partial(\rho\theta u_2)}{\partial \alpha_2}+\frac{\partial(\rho\theta u_3)}{\partial \alpha_3}-\frac{1}{J}\frac{\partial\left(\frac{\rho\kappa_h}{J}\frac{\partial\theta}{\partial \alpha_1}\right)}{\partial \alpha_1}-\frac{1}{J}\frac{\partial\left(\frac{\rho\kappa_h}{J}\frac{\partial\theta}{\partial \alpha_2}\right)}{\partial \alpha_2}-\frac{\partial\left(\rho\kappa_v\frac{\partial\theta}{\partial \alpha_3}\right)}{\partial \alpha_3}\\
&+\frac{\rho}{R+\alpha_3}\left(2\left(\theta u_3-\kappa_v\frac{\partial\theta}{\partial \alpha_3}\right)-\frac{\alpha_1\theta u_1+\alpha_2\theta u_2}{2R}+\kappa_h\frac{\alpha_1\frac{\partial\theta}{\partial \alpha_1}+\alpha_2\frac{\partial\theta}{\partial \alpha_2}}{2RJ}\right).
\end{aligned}
\tag{A3}
$$

Appendix B: Vector Transformations

When initializing data fields (e.g., initial condition obtained from an prescribed value or a data assimilation process), or for vizualization purposes, it is necessary to transform the expression of vector fields from the Cartesian space to the stereographic space and vice versa. Consider a vector $\mathbf{v}$ whose Cartesian components are v_i^x, while they are v_j^α in the stereographic basis:

$$
\sum_{i=1}^{3} v_i^x\hat{\mathbf{e}}_i=\sum_{j=1}^{3} v_j^\alpha\hat{\mathbf{g}}_j \tag{B1}
$$

The transformation from one space to the other is a rotation, which can be decribed by introducing the definition of the stereographic base vectors (2) in (B1):

$$
\sum_{i=1}^{3} v_i^x\hat{\mathbf{e}}_i=\sum_{j=1}^{3} v_j^\alpha\sum_{i=1}^{3} M_{j,i}\hat{\mathbf{e}}_i=\sum_{i=1}^{3}\sum_{j=1}^{3} v_j^\alpha M_{j,i}\hat{\mathbf{e}}_i \tag{B2}
$$

with

$$M=\frac{1}{4R^2+\alpha_1^2+\alpha_2^2}\begin{pmatrix} 4R^2-\alpha_1^2+\alpha_2^2 & -2\alpha_1\alpha_2 & \mp 4R\alpha_1 \\ -2\alpha_1\alpha_2 & 4R^2+\alpha_1^2-\alpha_2^2 & \mp 4R\alpha_2 \\ 4R\alpha_1 & 4R\alpha_2 & \pm\left(4R^2-\alpha_1^2-\alpha_2^2\right) \end{pmatrix}. \tag{B3}$$

Thanks to the orthogonality of the base vectors, we can easily deduce from (B2) the transformation of the components of **v** from the stereographic to the Cartesian basis:

$$v_i^x=\sum_{j=1}^{3} M_{j,i}v_j^\alpha. \tag{B4}$$

The transformation of the vector from Cartesian to stereographic coordinates can be found by inverting the relation (B4) which, in the case of a rotation, results in using the transposed matrix:

$$v_i^\alpha=\sum_{j=1}^{3} M_{i,j}v_j^x. \tag{B5}$$

Acknowledgments

The authors wish to thank Michael Baldauf who derived the analytical solution for the gravity waves test case and provided the C code used to compute it. Sébastien Blaise and Jonathan Lambrechts are Postdoctoral Researchers with the Belgian Fund for Research (F.R.S.-FNRS), while Eric Deleersnijder is an honorary Research Associate with the same institution. Computational ressources were provided by the Consortium des Équipements de Calcul Intensif (CÉCI), funded by F.R.S.-FNRS under grant 2.5020.11. Additional computing support from the National Center for Atmospheric Research (NCAR) has been made available through the project "Collaborative Research: A multiscale unified simulation environment for geoscientific applications," which is funded by the U.S.A. National Science Foundation under the Peta-apps grant 0904599. The present study was carried out in the framework of the project "Taking up the challenges of multi-scale marine modeling" which is funded by the Communauté Francaise de Belgique under contract ARC 10/15-028. No data were used in this paper. The test cases and analytical solutions are fully described in this document and cited literature.

References

Baldauf, M., D. Reinert, and G. Zängl (2014), An analytical solution for linear gravity and sound waves on the sphere as a test for compressible, non-hydrostatic numerical models, *Q. J. R. Meteorol. Soc.*, *140*(683), 1974–1985.

Bernard, P. E., J. F. Remacle, R. Comblen, V. Legat, and K. Hillewaert (2009), High-order discontinuous Galerkin schemes on general 2d manifolds applied to the shallow water equations, *J. Comput. Phys.*, *228*(17), 6514–6535.

Blaise, S., and A. St-Cyr (2011), A dynamic hp-adaptive discontinuous galerkin method for shallow-water flows on the sphere with application to a global tsunami simulation, *Mon. Weather Rev.*, *140*(3), 978–996.

Blaise, S., R. Comblen, V. Legat, J.-F. Remacle, E. Deleersnijder, and J. Lambrechts (2010), A discontinuous finite element baroclinic marine model on unstructured prismatic meshes. Part I: Space discretization, *Ocean Dyn.*, *60*(6), 1371–1393, doi:10.1007/s10236-010-0358-3.

Blaise, S., A. St-Cyr, D. Mavriplis, and B. Lockwood (2013), Discontinuous Galerkin unsteady discrete adjoint method for real-time efficient tsunami simulations, *J. Comput. Phys.*, *232*, 416–430.

Brdar, S., M. Baldauf, A. Dedner, and R. Klöfkorn (2013), Comparison of dynamical cores for NWP models: Comparison of COSMO and dune, *Theor. Comput. Fluid Dyn.*, *27*(3-4), 453–472.

Chen, Y., and H. L. Kuo (1986), A global model with overlapping mercator and stereographic grids, *Adv. Atmos. Sci.*, *3*(3), 302–313.

Chen, Y., R. Mittra, and P. Harms (1996), Finite difference time domain algorithm for solving maxwell's equations in rotationally symmetric geometries, *IEEE Trans. Microwave Theory Tech.*, *44*(6), 832–839.

Comblen, R., S. Legrand, E. Deleersnijder, and V. Legat (2009), A finite element method for solving the shallow water equations on the sphere, *Ocean Modell.*, *28*(1-3), 12–23.

Comblen, R., S. Blaise, V. Legat, J.-F. Remacle, E. Deleersnijder, and J. Lambrechts (2010), A discontinuous finite element baroclinic marine model on unstructured prismatic meshes. Part II: Implicit/explicit time discretization, *Ocean Dyn.*, *60*(6), 1395–1414, doi:10.1007/s10236-010-0357-4.

Côté, J. (1988), A Lagrange multiplier approach for the metric terms of semi-Lagrangian models on the sphere, *Q. J. R. Meteorol. Soc.*, *114*, 1347–1352.

Dennis, J. M., M. Levy, R. D. Nair, H. M. Tufo, and T. Voran (2005), Towards an efficient and scalable discontinuous Galerkin atmospheric model, in *Proceedings of the 19th IEEE International Parallel and Distributed Processing Symposium (IPDPS'05)—Workshop 13*, vol. 14, p. 7, IEEE Comput. Soc., Washington, D. C., doi:10.1109/IPDPS.2005.438.

Düben, P. D., P. Korn, and V. Aizinger (2012), A discontinuous/continuous low order finite element shallow water model on the sphere, *J. Comput. Phys.*, *231*(6), 2396–2413.

Giraldo, F. X., and M. Restelli (2008), A study of spectral element and discontinuous Galerkin methods for mesoscale atmospheric modeling: Equation sets and test cases, *J. Comput. Phys.*, *227*, 3849–3877.

Giraldo, F. X., J. S. Hesthaven, and T. Warburton (2002), Nodal high-order discontinuous Galerkin methods for the spherical shallow water equations, *J. Comput. Phys.*, *181*, 499–525.

Giraldo, F. X., M. Restelli, and M. Lauter (2010), Semi-implicit formulations of the navier-stokes equations: Application to nonhydrostatic atmospheric modeling, *SIAM J. Sci. Comput.*, *32*(6), 3394–3425.

Hesthaven, J. S., and T. Warburton (2008), *Nodal Discontinuous Galerkin Methods, Texts in Applied Mathematics*, vol. 54, Springer, N. Y.

Ivan, L., H. De Sterck, S. A. Northrup, and C. P. T. Groth (2013), Multi-dimensional finite-volume scheme for hyperbolic conservation laws on three-dimensional solution-adaptive cubed-sphere grids, *J. Comput. Phys.*, *255*, 205–227.

Jablonowski, C., and D. L. Williamson (2006), A baroclinic instability test case for atmospheric model dynamical cores, *Q. J. R. Meteorol. Soc.*, *132*, 2943–2975.

Jacobson, M. Z. (2005), *Fundamentals of Atmospheric Modeling*, Cambridge Univ. Press, Cambridge, U. K.

Kemmer, N. (1977), *Vector Analysis: A Physicist's Guide to the Mathematics of Fields in Three Dimensions*. Cambridge University Press, Cambridge, U. K.

Kent, J., P. A. Ullrich, and C. Jablonowski (2014), Dynamical core model intercomparison project: Tracer transport test cases, *Q. J. R. Meteorol. Soc.*, *140*(681), 1279–1293.

Koren, B., and K. Vuik (2009), *Advanced Computational Methods in Science and Engineering*, Springer Sci. & Business Media, Berlin.

Lamé, G. (1859), *Leçons sur les Coordonnées Curvilignes et leurs Diverses Applications*, Mallet-Bachelier, Paris.

Lauritzen, P. H., C. Jablonowski, M. A. Taylor, and R. D. Nair (2010), Rotated versions of the jablonowski steady-state and baroclinic wave test cases: A dynamical core intercomparison, *J. Adv. Model. Earth Syst.*, *2*, 15, doi:10.3894/JAMES.2010.2.15.

Majewski, D., D. Liermann, P. Prohl, B. Ritter, M. Buchhold, T. Hanisch, G. Paul, W. Wergen, and J. Baumgardner (2002), The operational global icosahedralHexagonal gridpoint model GME: Description and high-resolution tests, *Mon. Weather Rev.*, *130*(2), 319–338.

Marras, S., M. A. Kopera, and F. X. Giraldo (2014), Simulation of shallow-water jets with a unified element-based continuous/discontinuous Galerkin model with grid flexibility on the sphere, *Q. J. R. Meteorol. Soc.*, doi:10.1002/qj.2474.

Martinec, Z. (2003), *Continuum Mechanics*, University Lecture, Charles University in Prague, Prague. [Available at http://geo.mff.cuni.cz/vyuka/Martinec-ContinuumMechanics.pdf.]

Mayne, N. J., I. Baraffe, D. M. Acreman, C. Smith, N. Wood, D. S. Amundsen, J. Thuburn, and D. R. Jackson (2014), Using the UM dynamical cores to reproduce idealised 3-D flows, *Geosci. Model Dev.*, *7*(6), 3059–3087.

Mohseni, K., and T. Colonius (2000), Numerical treatment of polar coordinate singularities, *J. Comput. Phys.*, *157*, 787–795.

Murray, R. (1996), Explicit generation of orthogonal grids for ocean models, *J. Comput. Phys.*, *126*(2), 251–273.

Murray, R., and C. Reason (2002), Fourier filtering and coefficient tapering at the north pole in OGCMs, *Ocean Modell.*, *4*(1), 1–25.

Nair, R. D., and C. Jablonowski (2008), Moving vortices on the sphere: A test case for horizontal advection problems, *Mon. Weather Rev.*, *136*(2), 699–711.

Nair, R. D., S. J. Thomas, and R. D. Loft (2005), A discontinuous Galerkin global shallow water model, *Mon. Weather Rev.*, *133*, 876–888.

Park, S.-H., W. C. Skamarock, J. B. Klemp, L. D. Fowler, and M. G. Duda (2013), Evaluation of global atmospheric solvers using extensions of the jablonowski and williamson baroclinic wave test case, *Mon. Weather Rev.*, *141*(9), 3116–3129.

Phillips, N. A. (1957), A map projection system suitable for large-scale numerical weather prediction, *J. Meteorol. Soc. Jpn.*, *35*, 262–267.

Putman, W. M., and S.-J. Lin (2007), Finite-volume transport on various cubed-sphere grids, *J. Comput. Phys.*, *227*, 55–78.

Rahman, M. R. A. (2008), *High Order Finite Elements for Microsystems Simulation*, Cuvillier Verlag, Göttingen.

Rančić, M., R. J. Purser, and F. Mesinger (1996), A global shallow-water model using an expanded spherical cube: Gnomonic versus conformal coordinates, *Q. J. R. Meteorol. Soc.*, *122*(532), 959–982.

Ronchi, C., R. Iacono, and P. S. Paolucci (1996), The cubed sphere: A new method for the solution of partial differential equations in spherical geometry, *J. Comput. Phys.*, *124*(1), 93–114.

Sadourny, R. (1972), Conservative finite-difference approximations of the primitive equations on quasi-uniform spherical grids, *Mon. Weather Rev.*, *100*(2), 136–144.

Snyder, J. P. (1987), *Map Projections: A Working Manual*, U. S. Geol. Surv., Washington, D. C.

St-Cyr, A., and D. Neckels (2009), A fully implicit Jacobian-free high-order discontinuous Galerkin mesoscale flow solver, *Comput. Sci.*, *5545*, 243–252.

St-Cyr, A., C. Jablonowski, J. M. Dennis, H. M. Tufo, and S. J. Thomas (2008), A comparison of two shallow-water models with nonconforming adaptive grids, *Mon. Weather Rev.*, *136*, 1898–1922.

Straka, J. M., R. B. Wilhelmson, L. J. Wicker, J. R. Anderson, and K. K. Droegemeier (1993), Numerical solutions of a non-linear density current: A benchmark solution and comparisons, *Int. J. Numer. Methods Fluids*, *17*(1), 1–22.

Stuhne, G. R., and W. R. Peltier (2006), A robust unstructured grid discretization for 3-dimensional hydrostatic flows in spherical geometry: A new numerical structure for ocean general circulation modeling, *J. Comput. Phys.*, *213*(2), 704–729.

Stuhne, G. R., and W. R. Peltier (2009), An unstructured c-grid based method for 3-d global ocean dynamics: Free-surface formulations and tidal test cases, *Ocean Modell.*, *28*(13), 97–105.

Ullrich, P. A., T. Melvin, C. Jablonowski, and A. Staniforth (2013), A proposed baroclinic wave test case for deep- and shallow-atmosphere dynamical cores, *Q. J. R. Meteorol. Soc.*, *140*(682), 1590–1602.

Wood, N., et al. (2014), An inherently mass-conserving semi-implicit semi-Lagrangian discretization of the deep-atmosphere global non-hydrostatic equations, *Q. J. R. Meteorol. Soc.*, *140*(682), 1505–1520.

Zängl, G., D. Reinert, P. Rpodas, and M. Baldauf (2015), The ICON (ICOsahedral Non-hydrostatic) modelling framework of DWD and MPI-M: Description of the nonhydrostatic dynamical core, *Q. J. R. Meteorol. Soc.*, *141*(687), 563–579.